Radio Science, Volume 32, Number 1, Pages 127–151, January–February 1997

Evolution in polarimetric signatures of thin saline ice under constant growth

S. V. Nghiem, R. Kwok, and S. H. Yueh

Center for Space Microelectronics Technology, Jet Propulsion Laboratory, California Institute of Technology, Pasadena

A. J. Gow and D. K. Perovich

U.S. Army Cold Regions Research and Engineering Laboratory, Hanover, New Hampshire

J. A. Kong and C. C. Hsu

Department of Electrical Engineering and Computer Science and Research Laboratory of Electronics, Massachusetts Institute of Technology, Cambridge

Abstract. An experiment is carried out to measure polarimetric backscatter signatures at C band together with physical characteristics of thin saline ice grown at a constant rate under quiescent conditions. The objectives are to investigate the electromagnetic scattering mechanism in saline ice, to relate the polarimetric backscatter to ice physical characteristics, and to assess the inversion of ice thickness from backscatter data. Controlled laboratory conditions are utilized to avoid complicated variations in interrelated characteristics of saline ice and the environment. The ice sheet was grown in a refrigerated facility at the U.S. Army Cold Regions Research and Engineering Laboratory. Growth conditions, thickness and growth rate, temperatures and salinities, and internal and interfacial structures of the ice sheet were monitored. Measurements indicate that the laboratory saline ice has characteristics similar to thin sea ice in the Arctic. A strong increase of 6–10 dB is observed in backscatter as the ice grows from 3 to 11.2 cm in thickness. Ice characteristics and processes suggest that the large enhancement in backscatter relates to the interconnection and increase in the size of brine inclusions during the desalination process. Polarimetric signatures calculated with a physically based sea ice model agree with backscatter data at incident angles from 20° to 35° over the thickness range of the ice growth. Furthermore, backscattering coefficients of the saline ice sheet are shown to be similar to airborne radar measurements of thin sea ice growing in a newly opened lead in the Beaufort Sea. For the inversion the large increase in backscatter indicates that the ice thickness is retrievable for thin ice grown under the conditions in this experiment. More complicated conditions should be considered in future experiments to study their effects on the retrieval of sea ice parameters.

1. Introduction

The formation of sea ice impacts local and regional air-ice-sea interactions such as heat transfer and affects polar and global climate due to feedback mechanisms in the climate system [*Moritz et al.*, 1993]. Heat flux between ocean and atmosphere depends strongly on sea ice thickness. *Maykut* [1978] indicates that the net heat input to the cold atmosphere from sea ice in the thickness range of 0.0–0.4 m is up to 2 orders of magnitude larger than that from perennial ice. Even with a small areal coverage on the order of 1%, thin sea ice in leads starts to dominate the turbulent heat exchange and influences the boundary layer stability in the Arctic [*Maykut*, 1978].

For radar monitoring of thin ice in polar regions, scattering mechanisms need to be determined and related to sea ice physical and morphological characteristics to interpret and retrieve geophysical parameters from remote sensing data. This is necessary particularly for C band radars in view of the present European Remote Sensing Satellites 1 (ERS 1) [*European Space Agency* (*ESA*), 1992] and 2 (ERS 2); the Canadian RADARSAT [*Carsey*, 1993], which was successfully launched in November 1995; and the

Paper number 96RS03051.
0048-6604/97/96RS-03051$11.00

ENVISAT [*Gardini et al.*, 1995], planned for monitoring the polar ice caps and the sea ice extent. All of these sensors operate at C band frequencies with different incident angles and different polarizations (vertical polarization for ERS 1 and ERS 2, horizontal for RADARSAT, and both vertical and horizontal for ENVISAT).

C band polarimetric remote sensing data have been acquired by airborne synthetic aperture radars (SAR) for various ice types in the Beaufort Sea [*Cavalieri et al.*, 1991]. From this data set, polarimetric backscatter signatures of thin ice formed in newly opened leads are studied [*Nghiem et al.*, 1995b]; however, the ice thickness is not measured directly. It is very dangerous and costly to approach such active leads to measure in situ sea ice parameters for a prolonged time period. Backscatter from lead ice is also measured by spaceborne SAR such as ERS 1 [*Kwok and Cunningham*, 1994]; nevertheless, the satellite takes several days to approximately repeat the orbit and to observe the same lead again, and the environmental conditions corresponding to the later observation may have changed.

Laboratory environments provide controllable conditions, a safe and easy access, and a fine temporal resolution with a lower cost and a higher efficiency compared to field experiments. Laboratory experiments have been carried out to obtain radar signatures from thin saline ice; however, both ice properties and radar data at C band are limited. Backscatter of thin bare ice is measured [*Beaven et al.*, 1995] only for copolarized returns at several ice thicknesses, and important ice parameters are not available for different cases. C band polarimetric data are reported [*Onstott*, 1990] at a few isolated cases with different thicknesses, varied air temperatures, and modified surface conditions.

In this paper the purpose is to study the evolution in polarimetric radar backscatter signatures during the growth of thin sea ice in conjunction with ice properties at successive stages throughout the ice growth. The experiment was carried out by the Jet Propulsion Laboratory (JPL), the U.S. Army Cold Regions Research and Engineering Laboratory (CRREL), and the Massachusetts Institute of Technology (MIT) in September 1993. In this experiment (CRRELEX 1993) a saline ice sheet was grown in an indoor refrigerated facility at CRREL (referred to as the cold room hereafter) from open saline water at a constant growth rate under quiescent conditions. These simple controllable laboratory conditions, avoiding complicated variations in ice characteristics, allow for a definitive investigation of the dominant scattering mechanism and provide physical insights to electromagnetic wave interactions in the ice sheet.

A C band polarimetric scatterometer system was used to measure polarimetric signatures of thin saline ice at different incident angles. The system will be described later in this paper. Fully polarimetric backscatter data, consisting of all elements of the covariance or Mueller matrix [*Nghiem et al.*, 1990] as functions of incident angle, were taken together with ice characterization data. With measurements made at successive stages of the ice growth, this data set imposes physical constraints on the determination of the dominant scattering mechanism. A physically based model of polarimetric backscatter from sea ice relates the ice characterization parameters to the observed backscatter signatures. The full polarimetric data require that all curves of complete sets of polarimetric scattering coefficients have to be explained simultaneously by the scattering mechanism used in the theoretical model based on the available ice characterization data. Furthermore, model input parameters that characterize the scattering mechanism cannot be treated independently. These parameters are interrelated and governed by physical processes during the ice growth.

For the development of a sea ice thickness inversion model, the sensitivity of polarimetric scattering coefficients to ice thickness observed in this experiment provides an assessment of the thickness retrieval from backscatter data. In this respect the purpose of the experiment is to determine the fundamental feasibility of the thickness inversion under the simple controlled laboratory conditions. If it is feasible in this case, then more complicated conditions can be added in future experiments to investigate their effects on the inversion problem. To approach the problem by starting with all complicated environmental and meteorological field conditions will lead to difficulties in understanding the observations let alone the development of computational algorithms to retrieve sea ice parameters from remote sensing data.

Moreover, both physical characteristics and backscatter signatures of the saline ice grown in this experiment are compared with measurements of natural sea ice obtained from field experiments to determine the consistency of the laboratory saline ice with respect to Arctic sea ice. These comparisons bridge laboratory and field observations under similar conditions and serve as an evaluation of the feasibility to

use laboratory environments to investigate backscatter signatures for remote sensing of sea ice.

This paper is composed of 5 sections. The scatterometer system, experimental setup, and data collection are depicted in section 2. In section 3 the saline ice grown in the laboratory is described and compared with Arctic sea ice. The ice characterization includes growth conditions, thickness and growth rate, temperatures and salinities, and internal and interfacial structures of the ice sheet. Section 4 shows experimental observations of polarimetric signatures during the ice growth, reviews the sea ice theoretical model, and compares measured and calculated results. Section 5 summarizes the paper.

2. Experimentation

2.1. Scatterometer System

A schematic of the C band polarimetric scatterometer system is shown in the block diagram in Figure 1a. In this figure, shaded portions denote components located inside the cold room; all others are located outside. A computer is used to control the Hewlett-Packard network analyzer, relay actuator, disc drive, and printer. The system operates at a center frequency of 5 GHz over a bandwidth of 1 GHz. Step-frequency signals are transmitted from the network analyzer through the RF subsystem to the antenna.

The RF subsystem consists of a low-noise RF amplifier, polarization switches, and other components whose temperature is regulated at 25°C with a temperature processor. The relay actuator switches polarizations of transmitted and received waves to all combinations in the linear polarization basis to measure full complex scattering matrices. The antenna is a dual-polarization diagonal horn with a beamwidth of 12° and a peak gain of 22.6 dBi at the center frequency. Data in the frequency domain are collected and processed with a fast Fourier transform technique to select signals received from target ranges. The antenna is mounted on a positioner capable of pointing the look direction to all incident angles (0°–180°, where 0° corresponds to downward vertical direction and 180° is the upward vertical direction) and all azimuthal angles (0°–360° for the full-circle pointing capability). The system has three operating modes: a quick-look mode for testing, a calibration mode, and a data acquisition mode. Further details of data processing, calibration, and antenna characteristics are presented in the appendices.

2.2. Experimental Setup

The ice sheet was grown in a two-story cold room. The lower story contained a 1.2-m-deep pool covering an area of approximately 5 by 7 m. The antenna was set at about 3 m above the ice surface to ensure the far-field condition of the antenna. Microwave absorbers were deployed to minimize unwanted reflections and multipath effects. Calibration targets such as trihedral corner reflectors and a metallic sphere were positioned on a Styrofoam pedestal with the background covered by absorbers. The antenna positioner, shown in Figure 1b, was balanced using the horizontal level control above the base to within 0.02° with respect to the gravitational horizontal plane. This plane was used as the reference to set the normal incident angle. The temperature-controlled RF subsystem and the antenna were mounted on the same frame and thus were stationary with respect to each other. Figure 1b illustrates the arrangement of the antenna, the RF subsystem, and the positioner. Two RF cables took input and output signals from inside the cold room out to the controlling system. With frequency converters, signals in and out of the RF subsystem were converted to low-frequency base band, ensuring better phase coherency and low loss in the cables.

Outside the cold room the control system, including the network analyzer, the computer and disc drive, relay actuator, and angle controllers, was arranged on a desk. With this setup the operator of the polarimetric scatterometer sent all commands from outside and did not need to enter the cold room during scatterometer measurements of the ice sheet. Operating under Hewlett Packard-Basic software in the computer, the network analyzer transmitted and received RF signals from the subsystems inside the cold room, and the data, including amplitudes and phases, were compressed and recorded on the hard disk and backed up by the disk drive. Polarization switches and the relay actuator automatically turned the polarizations of transmitted and received waves for full polarimetric measurements. The antenna was pointed to desired angles by two separate remote controls: one for incidence and the other for azimuth. A digital inclinometer, whose calibration was checked with a precise mechanical inclinometer with an accuracy of 0.02°, determined incident angles to within an angle resolution of 0.05°. The angles were shown on a digital display located on the desk next to the computer and the angle controllers.

The cold room temperature was controlled with a

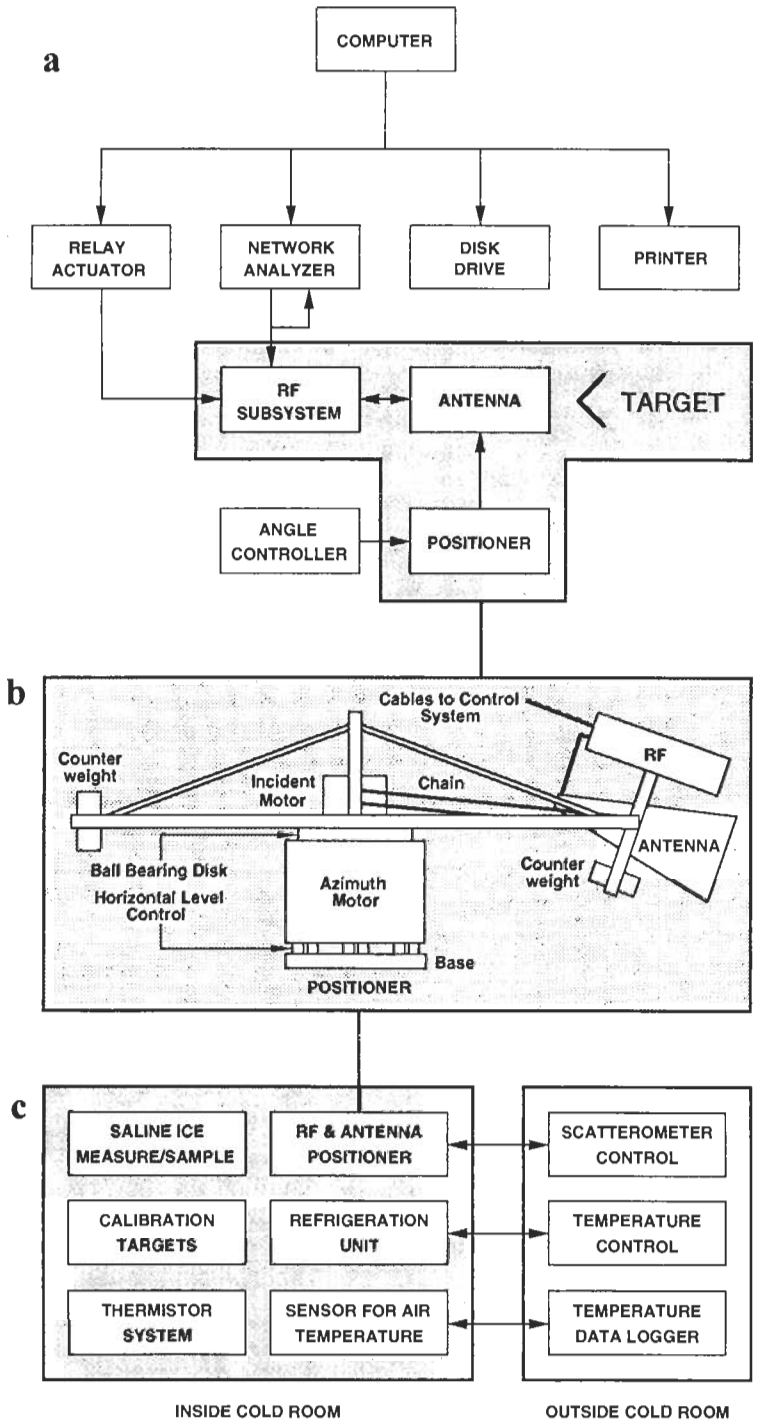

Figure 1. Experimental setup: Shaded portions denote components inside the cold room. (a) Polarimetric scatterometer system. (b) Positioner arrangement with the antenna and the RF subsystem. (c) Summary of the experimental setup inside and outside the cold room.

thermostat, and air temperatures were taken and recorded on a data logger outside the room. A thermistor string was inserted in the water at the beginning of the experiment and remained in place during the ice growth. This device measured profiles of air temperature above the ice surface, ice temperature as a function of ice depth, and water temperature below the interface. Thermistor string temperature data were recorded in a logger inside an insulated box. To minimize temperature perturbations, we entered the cold room only for short periods of time to carry out ice thickness measurements, surface roughness characterization, and ice sampling. The block diagram in Figure 1c summarizes the experimental setup discussed above.

2.3. Data Collection

During the saline ice growth, the polarimetric scatterometer was used to collect backscatter data as a function of ice thickness at increments of about 1 cm. Polarimetric measurements were made for incident angles between 0° to 45°, each with three to five independent azimuthal angles. At each azimuthal direction and incident angle, a full polarimetric scattering matrix, containing four complex elements, was measured. The Fourier technique is used to transform the data into the time domain where reflections from RF system, antenna, and some contaminations from the surroundings are eliminated and backscatter from the saline ice sheet is isolated for further data processing. The polarimetric data processor involves data decompression, system noise removal, windowing, Fourier transforms, time gating, system transfer function computation, signal reconstruction, ensemble averaging, three-dimensional antenna pattern characterization, backscatter deconvolution, polarimetric calibration, and radiometric calibration (see Appendix A).

In the final format the data are presented in terms of polarimetric backscattering coefficients, which are elements of the polarimetric covariance matrix, including conventional copolarized backscattering coefficients σ_{hh} and σ_{vv}, cross-polarized return σ_{hv}, and polarimetric complex correlation σ_{hhvv} including magnitude and phase. Alternatively, polarimetric data are also reported in normalized forms: $\gamma = \sigma_{vv}/\sigma_{hh}$, $e = \sigma_{hv}/\sigma_{hh}$, and $\rho = \sigma_{hhvv}/(\sigma_{hh}\sigma_{vv})^{1/2}$ [*Nghiem et al.*, 1990]. Copolarized and cross-polarized fields are not correlated owing to the azimuthal symmetry of the ice sheet [*Nghiem et al.*, 1992, 1993b]; data for cross-correlated backscattering coefficients σ_{hhhv} and σ_{hvvv} fall to the measurement noise floor. Measured data for off-diagonal elements (hv and vh) in the scattering matrix were equivalent to within 0.15 dB in magnitudes and 3° in phases, which showed that the system satisfied the reciprocity condition very well. Polarimetric scattering data are used to obtain Mueller matrices and polarization signatures characterizing polarimetric scattering properties of the saline ice sheet. Full scattering matrix measurements of trihedral corner reflectors, the metallic sphere, and their backgrounds were taken for system calibrations.

To characterize the ice sheet and its environment, physical property measurements of air, ice, and water were made in conjunction with the polarimetric scatterometer data. Air temperature data were taken every 5 min. Vertical profiles of air, ice, and water temperatures were recorded throughout the experiments. Ice samples were taken from the ice sheet before each set of scatterometer measurements for thickness measurements, salinity profiles, and internal ice structure study. Scrapings from the top surface of the ice sheet were taken periodically for surface salinity measurements. A mechanical roughness profiler was also used to obtain surface roughness measurements. The polarimetric scatterometer measurements and the physical characterization data constitute the basis for the analysis in this paper.

3. Saline Ice Growth

In this section the growth of the ice sheet from saline water is described. Measured results for physical characteristics of the ice sheet grown from saline water are presented. Results of field measurements of Arctic sea ice are also shown for comparison with those obtained from the laboratory-grown saline ice. These observed characteristics will be utilized to analyze the evolution in polarimetric signatures during thin saline ice growth.

3.1. Growth Conditions

The ice sheet was grown from saline water with a salinity of 32‰ under quiescent conditions without wind and wave actions. Initially, the water was spray seeded to stimulate growth of more typical columnar ice [*Gow et al.*, 1987]. Columnar ice constitutes a major fraction in the global sea ice mass [*Weeks and Ackley*, 1982]. Under these growth conditions the ice sheet was dominated by columnar crystal ice with c axes parallel to the horizontal plane. The c axes were distributed randomly within the horizontal plane in the absence of water current underneath the ice

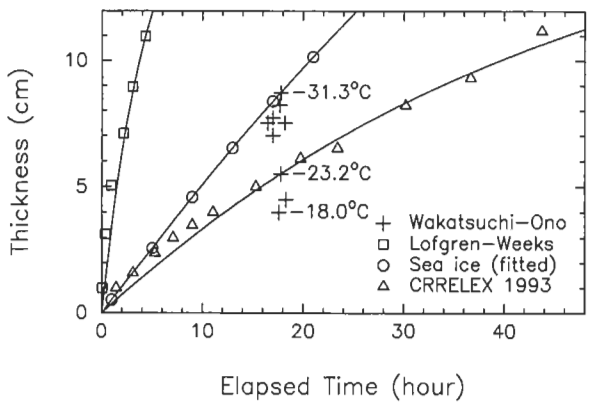

Figure 2. Thin ice growth from saline water: Plusses are field measurements from Barrow, Alaska, under various air temperatures for sea water at near 33‰ salinity obtained by *Wakatsuchi and Ono* [1983], squares are for ice grown at −70°C from water of 30‰ salinity by *Lofgren and Weeks* [1969], circles are for sea ice formed under cold Arctic winter conditions obtained by a fit of results by *Thorndike et al.* [1975], and triangles are for saline ice grown in the CRREL cold room at −21.8°C air temperature from water of 30‰. Exponential fits are represented by continuous curves.

sheet. Air and water temperatures were both kept constant during the ice growth. Air temperature was −21.8°C and water temperature was −2.0°C. Data indicate that the temperatures remained constant with a mean square deviation of 0.1°C throughout the saline ice growth. A closely linear growth with a nearly constant rate was maintained throughout the duration of the experiment.

3.2. Thickness and Growth Rate

The ice sheet attained a thickness of 11 cm in 2 days. Ice thickness measurements were taken mostly near the area outside the antenna footprints corresponding to small incident angles. Ice thickness was also measured across the entire ice sheet at the end of the experiment when the radar measurements were completed. Figure 2 presents the thickness as a function of time. The symbols represent thickness data, and the continuous curves are exponential fits of the data. These cases are actually quite well represented by linear functions under the first-order expansion in a Taylor series because the exponents are very small for the elapsed time under consideration. The initial time reference corresponds to the time when the seeding was done. Measured results from our experiment denoted with triangles reveal a linear relationship between thickness and time. In fact, our experimental data are fitted very well with the linear relation

$$h(t) = 1.2 + 0.23t \qquad h < 12 \text{ cm} \tag{1}$$

for thickness $h(t)$ (centimeters) versus time t (hours) with a high correlation coefficient of 0.996, which is higher than the correlation coefficient corresponding to the exponential fit. Equation (1) gives a constant growth rate of $v = dh/dt = 0.23$ cm/h, or 6.4×10^{-5} cm/s, throughout the experiment. The initial thickness offset in (1) is caused by uncertainties in the linear fitting of the measured data and in the initial spray-seeded growth conditions.

The linear growth behavior of thin sea ice observed in this experiment is consistent with heat transfer equations for ice growth. The differential equations governing the ice growth consist of both the heat convection and the heat conduction terms [*Adams et al.*, 1991]. For young thin ice the convection effect dominates, the growth rate is nearly constant, and the ice growth is approximately linear. With typical thermophysical parameters the heat conduction can balance only with the heat convection at a thickness of 0.4 m, and even at the thickness of 1.2 m like thick first-year sea ice, the convection still accounts for 25% of the freezing time [*Adams et al.*, 1960]. Thermophysical parameters reported by *Adams et al.* [1960], *Yen*, [1981], and *Fukusako* [1990] together with the ice growth equation closely predict the result obtained above. It is interesting to note that the thickness of 0.4 m is coincident with the thickness at which an abrupt change occurs in the slope of *Cox and Weeks*'s [1974] desalination curve.

The experimental data are compared with results from other laboratory studies, typical sea ice growth under cold winter conditions, and actual sea ice field measurements, as shown in Figure 2. For reference, *Lofgren and Weeks*'s [1969] laboratory results of ice grown at a very fast rate from saline water with an initial salinity of 30‰ are plotted with the squares. The temperature at the ice surface was −70°C, which is much colder than the case of our experiment and that of Arctic sea ice. For sea ice growing under conditions typical of polar oceans, *Thorndike et al.* [1975] estimated sea ice growth rate as a function of time throughout the year. Under cold winter conditions in March the growth rate is relatively high for Arctic sea ice at frigid air temperatures and the thickness [*Nghiem et al.*, 1995a]

$$h(t) = 60[1 - \exp(-0.2116t/24)] \qquad h < 50 \text{ cm} \tag{2}$$

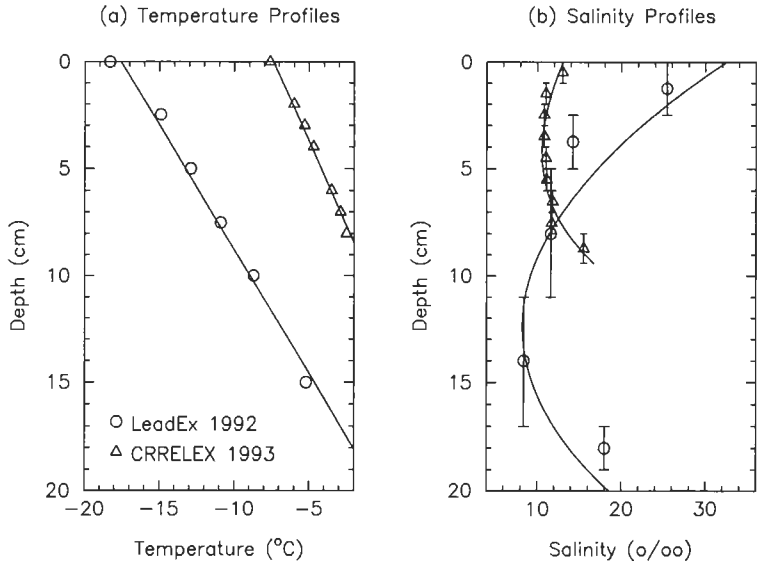

Figure 3. (a) Temperature and (b) salinity profiles of laboratory-grown saline ice denoted with triangles (CRRELEX 1993) and sea ice in a new lead denoted with circles (LeadEx 1992). Both ice types are characterized by typical linear temperature distributions and C-shaped salinity profiles.

is obtained from a fit of Thorndike et al.'s results. This growth for thin ice is linear under the first-order expansion, and the corresponding thickness calculated from (2) is plotted with the circles in Figure 2.

A field experiment was carried out at Barrow, Alaska, by *Wakatsuchi and Ono* [1983] for sea ice grown at various temperatures from seawater with salinities near 33‰. In Figure 2, *Wakatsuchi and Ono*'s [1983] data of sea ice are represented by the pluses, which span a range of thicknesses at different growth rates. The slowest growth was at an air temperature of −18.0°C. In the intermediate case of −23.2°C for air temperature, the growth rate of sea ice is very similar to the result we obtained under the controlled air temperature of −21.8°C, which is close to the temperature condition of the field experiment. In the case of a more rapid growth at the cold temperature of −31.3°C, the sea ice thickness is close to the above estimation given by (2) under Arctic cold winter conditions.

3.3. Temperatures and Salinities

Temperature and salinity profiles of the saline ice sheet are presented in Figure 3, where they are compared with profiles of young lead ice in the Beaufort Sea obtained from the LeadEx Experiment in 1992 [*LeadEx Group*, 1993]. The LeadEx ice sample is thicker than the saline ice sample from our experiment. Figure 3 shows that the linear temperature profile and the C-shaped salinity profile of the saline ice are characteristically similar to the temperature and salinity profiles of the LeadEx ice, respectively. These profiles are typical of young Arctic sea ice. Surface salinity measured from surface-scraped samples collected during the growth of the saline ice sheet is 49 ± 7‰ independent of ice thickness.

Bulk salinities of the ice sheet were measured from ice samples periodically retrieved during the ice growth experiment. Measured results, plotted with triangles in Figure 4, reveal a desalinization of the ice sheet that reduces the salinity by 30%. The data are fitted with a linear curve with a negative slope characterizing the desalinization. For comparison with the desalinization observed in Arctic sea ice, results from *Cox and Weeks* [1974] are plotted with circles in Figure 4. The salinity data for sea ice were assembled by *Cox and Weeks* [1974] from field experiments in the Beaufort, Bering, and Labrador Seas and in Viscount Melville Sound carried out from 1955 to 1972 [*Cox and Weeks*, 1974]. The desalinization effect in the saline ice compares well with that of natural sea ice. Although the desalinization rate of the saline ice seems to be faster than that of sea ice, the difference in the salinities is within the uncertainty of field measurements. It should be noted that the desalinization rate or the slope of the salinity function of the saline ice is for the laboratory conditions, whereas the

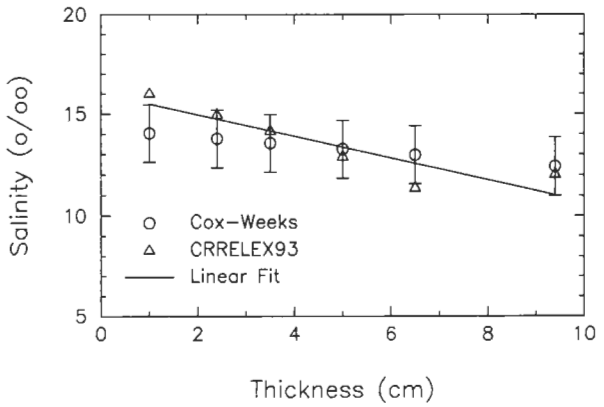

Figure 4. Bulk salinity in ice: Triangles are for CRRELEX 1993 saline ice data with a linear fit plotted with the continuous line, and circles are for Arctic sea ice. The decreasing trend of salinity with thickness indicates the desalination occurring during the ice growth process.

field salinity in Figure 4 represents average values over a wide variety of field conditions. Thus, while it is reasonable to indicate that the laboratory case fits within the range of the field salinity data, it is not compatible to compare the salinity slope of the saline ice under this particular realization with the average field value.

3.4. Internal and Interfacial Structures

Internal crystal structures are studied with thin sections cut vertically and horizontally to provide a three-dimensional view. The technique of preparing a thin ice section on a histological microtome was presented by *Gow and Weeks* [1977]. Vertical and horizontal thin sections of ice are shown in Figure 5 to compare internal structures of the laboratory and the Arctic (LeadEx) ice. The scale of the vertical sections is about 80% of the actual size, and that of the horizontal sections is magnified, as indicated by the millimeter markings on the margins of the photographs.

For the laboratory saline ice there is a thin transition layer where ice crystals are randomly oriented, as seen in the upper part of the vertical section in Figure 5. Beneath this layer, ice crystals become elongated in the vertical direction and the c axes become oriented in parallel to the horizontal plane. As both vertical sections in Figure 5 indicate, the vertical columnar structures of the laboratory-grown ice and LeadEx ice are similar. The horizontal thin section of laboratory ice shows elongated cross sections of ice platelets sandwiching brine inclusions which appear as small dark pockets in the horizontal section image. The multiplatelet nature of individual crystals is clearly demonstrated in the horizontal sections in Figure 5. These crystals, however, are randomly oriented in the horizontal plane and so are the corresponding c axes. Similar horizontal structures are seen in the LeadEx horizontal thin section.

At the interface between ice and water, ice platelets project into water to form parallel rows of knife-edge grooves in each cellular grain growing under conditions of the constitutional supercooling [*Lofgren and Weeks*, 1969]. Brine entrapped between adjacent ice platelets leaves a permanent record of the positions of intercellular grooves [*Lofgren and Weeks*, 1969]. The distance between the midpoints of adjacent grooves is defined as the brine layer spacing or the cellular substructure spacing. *Lofgren and Weeks* [1969] showed that the average cellular substructure spacing a_0 inversely depends on the growth rate v according to the following relationship:

$$\log (a_0 v) = \log A + n\left(\log \frac{1}{v}\right)^2 \tag{3}$$

where log is the logarithm of base 10, a_0 is in centimeters, v is in centimeters per second, $\log A = -4.069$, and $n = -0.093$. This inverse relation is plotted in Figure 6 together with experimental data taken by *Lofgren and Weeks* [1969].

From horizontal thin sections taken near the ice-water interface at different thicknesses during the laboratory experiment, we found that $a_0 = 3.6 \times 10^{-2}$ cm within an uncertainty of 15% at all thicknesses where horizontal sections are available. This observation agrees well with (3), which indicates that a_0 depends primarily on v. Since the growth rate remained practically constant during the ice growth as discussed in section 3.2, the value of a_0 should be constant. For the growth rate of 0.23 cm/h, or equivalently $v = 6.4 \times 10^{-5}$ cm/s, $\log^2 (1/v) = 17.6$ and $\log (a_0 v) = -5.6$. Our laboratory result is represented by the triangle in the plot of Figure 6. The CRRELEX result compares very well with the *Lofgren and Weeks* [1969] curve and data. Results from LeadEx measurements of a_0 and v are also plotted with circles in Figure 6 for comparison. LeadEx results are consistent with Lofgren and Weeks's results to within the measurement uncertainty. Furthermore, the cellular substructure spacings of laboratory grown and LeadEx ice are practically the same at similar growth rates (see Figure 6). A study of first-year sea ice also shows the inverse

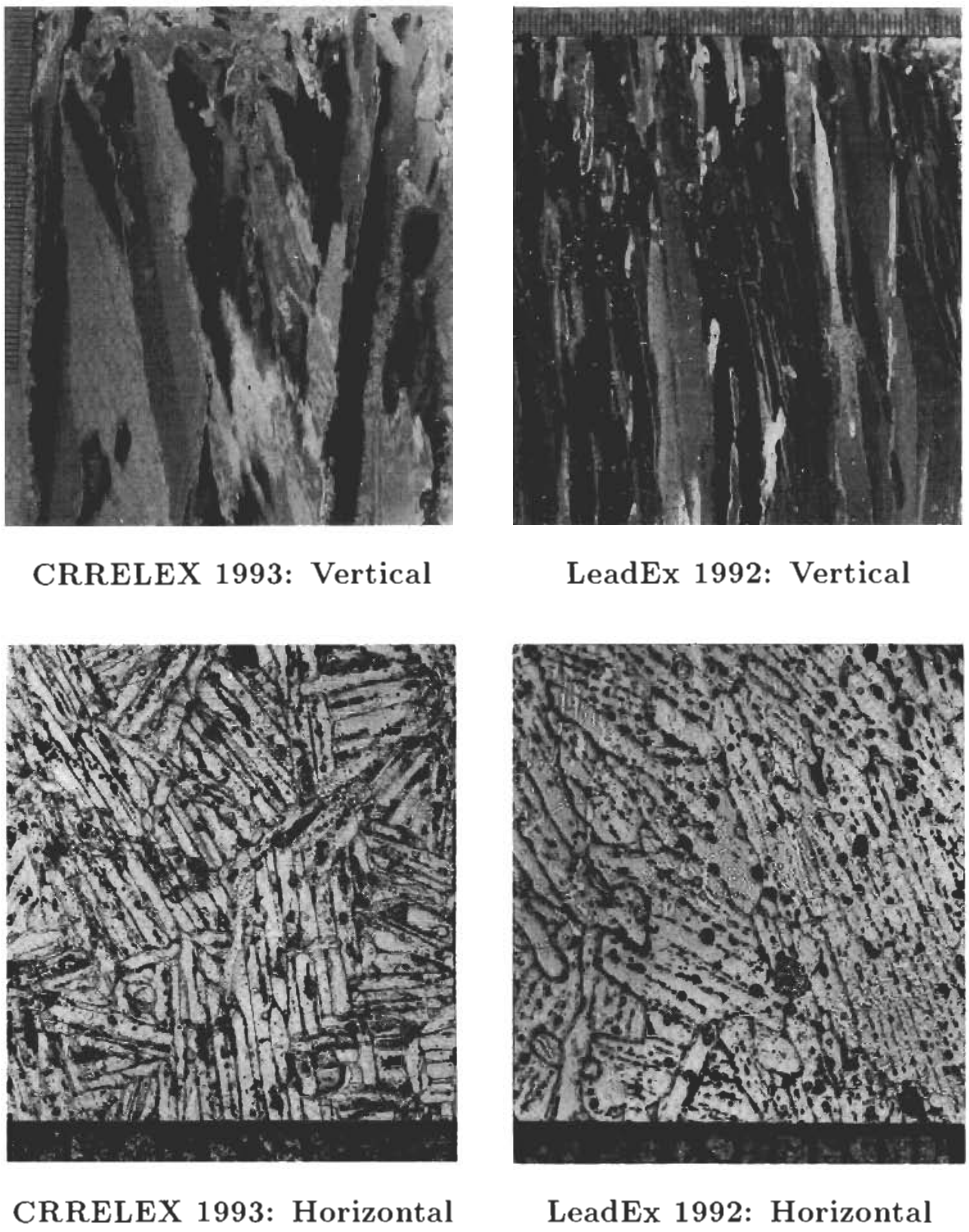

Figure 5. Vertical and horizontal thin sections of saline ice (CRRELEX 1993) and sea ice growing in a new lead (LeadEx 1992).

relation between spacing and growth rate [*Nakawo and Sinha*, 1984].

A 1-m-long roughness profiler, shown in Plate 1, was used to measure the surface roughness of the air-ice interface. The profiler consists of a row of vertical pins mounted on a frame made of light and rigid material. We developed a method of relative calibration for the roughness measurements. First, a long piece of lightweight material with a perfectly flat glassy surface is placed on the ice surface and beneath the pins, as seen in Plate 1a. A high-resolution photograph is taken, and positions of the pin heads represent the perfectly smooth surface to be used as the reference (Plate 1a). Then the long piece is removed to allow the pins to touch the ice surface without disturbing the position of the profiler. Note

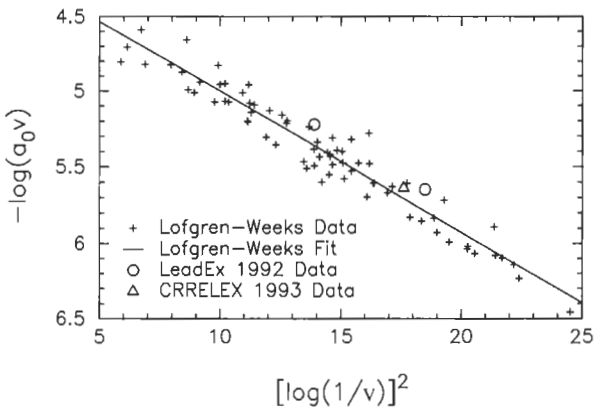

Figure 6. Relationship between cellular substructure spacing and growth rate: Crosses are for experimental data from *Lofgren and Weeks* [1969] with the continuous line for the linear fit, circles are for sea ice from LeadEx data, and the triangle is for saline ice grown at CRREL.

that the profiler is not attached to the long piece in any way. The initial position of the camera is maintained, and another picture of the profiler is taken with the pin head positions containing information of the ice surface roughness (Plate 1b).

The two photographs are enlarged to determine the differences by subtracting the pin head positions between the two cases. This yields the actual roughness calibrated against the perfectly flat surface. Note that this method depends only on relative positions and not on absolute height measurements of the pin heads. Since the ice in this experiment was grown under quiescent conditions, the surface was very smooth and appeared mirror-like, as seen in Plate 1. This condition was retained during ice growth, and the ice surface was not artificially perturbed at any time. Several surface measurements were carried out during the experiment, and the results do not show any noticeable variation in the surface roughness to within the limitations of 0.1 mm for height resolution and 2.8 cm for surface correlation length in this surface measurement method.

4. Polarimetric Signatures

4.1. Experimental Observations

Polarimetric backscatter data are presented in Figures 7 and 8 together with model results as functions of incident angle and ice thickness. Measured data for σ_{hh}, σ_{vv}, and σ_{hv} in Figure 7a show a slightly decreasing trend in all of these backscattering coefficients as functions of incident angles ranging from 20° to 35°. The decrease in backscatter is only within 2 dB in the range of incident angle under consideration. In Figure 7b, data for magnitude of the complex correlation coefficient ρ between horizontal and vertical returns are between 0.8 and 0.9 except at 35° the value goes down to approximately 0.7. Data in the bottom panel for phase of ρ have small negative values. The correlation coefficient ρ is not very sensitive to incident angle in the range shown in Figure 7. Similar trends are observed for backscatter of the saline ice sheet at other thicknesses; for instance, see backscatter data for the same ice sheet at a thickness of 11.2 cm from *Nghiem et al.* [1995c, Figure 13].

A large increase of 6–10 dB is observed in backscatter data in Figure 8 for σ_{hh}, σ_{vv}, and σ_{hv} at incident angles from 20° to 35° when the saline ice grows from 3 to 11.2 cm. These results indicate that backscatter is quite sensitive to ice thickness under the constant growth and quiescent conditions. In general, measured values of σ_{hh} and σ_{vv} are close to each other except that in certain isolated cases σ_{vv} is larger than σ_{hh} (see Figure 8). Cross-polarized backscattering coefficients σ_{hv} and σ_{vh} are compared well to within a fraction of a decibel; this serves as a check of the reciprocity of the system, and only σ_{hv} is presented in Figure 8. The cross-polarized return is observed to be on the order of 10 dB lower than the copolarized backscattering coefficients, all showing the strong increasing trend with ice thickness. The significance of this result is that the ice thickness can be retrieved from remote sensing backscatter measurements, at least for the configuration and ice characteristics in this experiment. An inverse algorithm using the Levenberg-Marquardt optimization technique [*Marquardt*, 1963; *Kuester and Mize*, 1973] can be applied to these time series backscatter measurements to retrieve the ice thickness [*Shih et al.*, 1996]. However, effects of more complicated conditions of sea ice growth, such as diurnal variations on the retrieval of ice thickness, should be investigated in future experiments.

4.2. Scattering Mechanisms

Backscatter from the saline ice sheet is caused by different mechanisms, including (1) scattering from surface roughness at the air-ice interface, (2) scattering from the knife-edge grooves at the ice-water interface, or (3) scattering from inhomogeneities such as brine inclusions in the ice sheet. Polarimetric backscatter observations together with ice character-

ization measurements are used, not in isolated cases but appropriately treated as successive stages during the process of the saline ice growth, to identify the dominant scattering mechanism of electromagnetic waves in the saline ice configuration.

4.2.1. Scattering from the air-ice interface. First suppose that the surface-scattering mechanism at the air-ice interface is dominant. In this case the smooth condition of the ice surface seen in Plate 1 renders the scattering characteristics of the Kirchhoff approximation or the small perturbation method in the range of small incident angles under consideration. Under this condition the surface backscatter is characterized by a large decrease with incident angle, a cross-polarized return much smaller than the copolarized backscatter, and a correlation coefficient ρ close to unity [*Nghiem et al.*, 1995a]. These characteristics are all contradictory to the experimental observations shown in Figure 7. Furthermore, rough surface measurements described in section 3.4 indicate that the surface is so smooth that the roughness is not measurable with the profiler limitations. For an ice surface smoother than that, backscatter is more than 10 dB lower than the measured data. All of the above arguments are based on Kirchhoff or small-perturbation surface-scattering models [*Tsang et al.*, 1985; *Nghiem et al.*, 1995a].

Now we examine the surface scattering mechanism from experimental observations themselves. Backscatter data in Figure 8 show an increase as much as 10 dB during the ice growth. This increase requires the surface roughness to increase significantly with the ice thickness, which is not supported by the experimental observations described in section 3.4. An increase in surface salinity also results in an enhancement of the surface scattering. To achieve the 10-dB increase, the surface salinity would need to be strongly increased; instead, measurements show that the salinity was at 49 $\pm$ 7‰ independent of ice thickness during the ice growth as presented in section 3.3. An increase in effective permittivity of the ice sheet also makes the permittivity contrast between air and saline ice larger and gives rise to higher surface backscatter. However, this would require a salinity increase in the ice sheet which is contradictory to the observed desalination indicated by the bulk salinity decrease shown in Figure 4.

4.2.2. Scattering from the ice-water interface. At the ice-water interface, knife-edge grooves of ice platelets protruding into water may scatter electromagnetic waves. All surface-scattering models assuming a small slope for the roughness are not applicable in this case because the grooves have a steep slope. In view of the Floquet-mode scattering [*Kong*, 1986] the cellular substructure spacing between the grooves is much smaller than the wavelength at 5 GHz, and all modes become evanescent except the zero mode, which propagates in the same forward direction of waves reflected by a planar interface. Note that the wavelength is still in the centimeter range even if the layer near the ice-water interface is assumed to contain mostly saline water. Thus the wavelength is still much larger compared to the submillimeter scale of the intercellular grooves. This mechanism suggests that the scattering from the grooves at the interface should not contribute significantly to the backscatter; however, this surface may yield some scattering since the groove domains are finite and nonuniform.

We use experimental observations again to examine the scattering from the ice-water interface. Equation (3) requires that the structure at this interface does not change as the ice grows at a constant rate. This is supported by the fact that measured values for a_0 remained at 3.6×10^{-2} cm during the ice growth as discussed in section 3.4. The unchanged interfacial morphology would give the same backscatter if the ice sheet were lossless. In contrast, the saline ice is lossy. As the ice thickness increases nearly four-fold, from 3 cm to 11.2 cm, the two-way attenuation (waves downgoing into the ice sheet and upgoing toward the scatterometer) in the saline ice should decrease the backscatter in the decibel domain by several times since the attenuation is an exponential function of the path length. This is again quite contradictory to the observed increase of up to 10 dB in the backscatter data shown in Figure 8.

4.2.3. Scattering from volume inhomogeneities. The plots of experimental data in Figure 8 show that the measured backscatter correlates with the increase in thickness of the saline ice sheet during the ice growth at all incident angles under consideration. This suggests an investigation into the relationship of the scattering mechanism to scatterers within the volume of the ice sheet.

A simple consideration is that the number of such scatterers increases as the ice grows thicker, and thus the backscatter becomes larger. However, the 10-dB backscatter increase cannot be obtained with an approximately four-fold increase in thickness even under the extreme assumptions of incoherent summing of all scattering from individual scatterers and ignoring additional scattering loss with a longer two-

a)

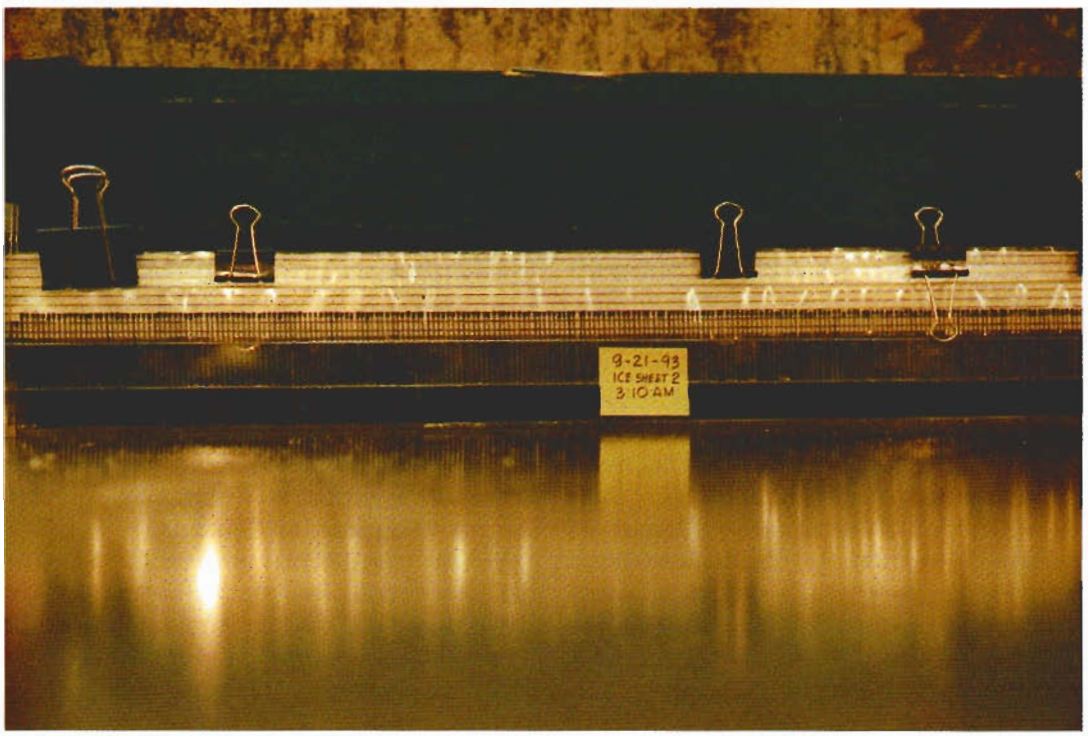

b)

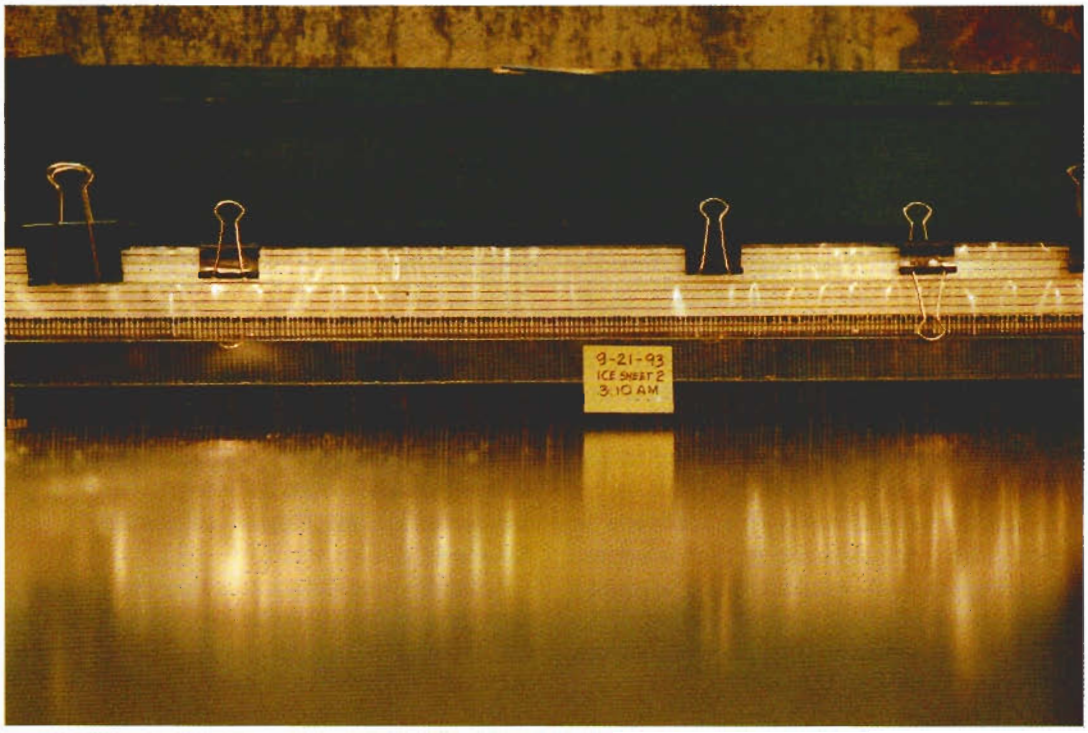

Plate 1. Photographs of the profiler for surface roughness measurements. (a) Reference position with the pins standing on a perfectly smooth surface of a thin piece of glassy material. (b) Position with the pins touching the ice surface with the long glassy piece removed. The differences of pin head positions of the two cases represent the surface roughness.

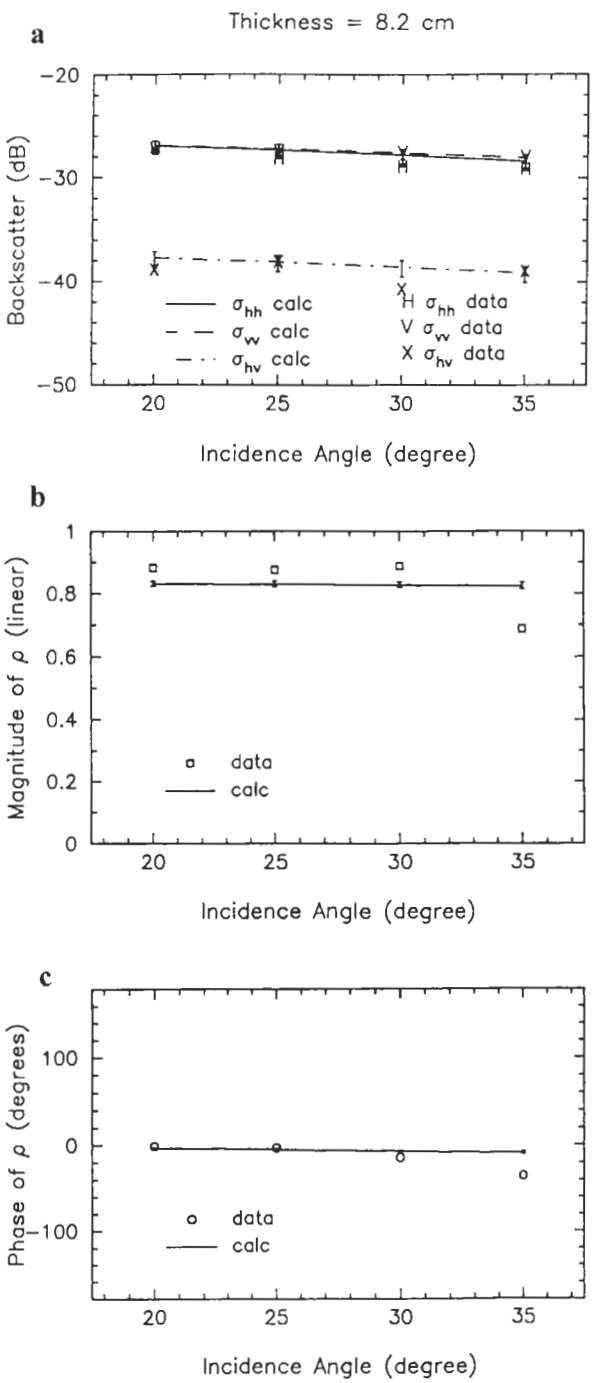

Figure 7. Measured data and calculated results for polarimetric backscattering coefficients as functions of incident angle for the 8.2-cm-thick saline ice sheet. (a) Backscattering coefficients σ_{hh}, σ_{hv}, and σ_{vv}. (b) Magnitude of the complex correlation coefficient ρ between horizontal and vertical returns. (c) Phase of the complex correlation coefficient ρ. Calculated results are obtained with a Gaussian distribution of ice thickness with ± 1°C uncertainty in ice temperature.

way path length for a larger ice thickness; the loss will limit the increase much below the four-fold factor. Thus there must be some processes, taking place in the ice volume, which alter physical characteristics of the scatterers, giving rise to a larger backscatter increase during the ice growth. Temperature and salinity are the two major factors determining saline ice characteristics. Since air and water temperatures remained constant, the temperature in the ice sheet did not change significantly during the experiment.

A factor that remains to be considered is that of the effects of processes related to salinity in the ice sheet. During the ice growth, desalination takes place (see Figure 4) and the bulk salinity can be reduced by several desalination mechanisms [*Weeks and Ackley*, 1982]: surface flushing, expulsion, migration, and gravity drainage. Surface flushing requires meltwater on the sea ice surface. This mechanism could not have happened in this particular experiment because the ice surface temperature was always kept well below freezing.

Brine expulsion occurs when ice temperatures decrease, causing liquid brine inside the pocket to freeze to the pocket wall. Some brine is thereby forced out since the specific volume of ice is about 10% larger than that of water. In general, brine expulsion may contribute to the total desalinization. The ice sheet in this experiment, however, was grown at constant air and water temperatures with a linear temperature profile, resulting in a stable average ice temperature. Under this condition the brine expulsion is weaker compared to the case where the ice sheet is grown under a quickly decreasing air temperature. Since backscatter is larger for larger brine pockets, the backscatter increase does not support the dominance of the wall freezing effect, which reduces the size of brine inclusions, on microwave scattering. *Cox* [1974] finds that expulsion is not the dominant contributor to the desalination except for the first few hours of sea ice growth.

Brine migration is caused by the diffusion through a temperature gradient between cold air and warm seawater. For brine pockets in the micron range, the diffusion coefficient is small and the corresponding migration rate is small and does not depend on pocket size [*Kingery and Goodnow*, 1963]. However, for brine pockets in the millimeter range, convection is possible and the effective diffusion can be 3 orders of magnitude larger; as a result, the migration rate is significantly enhanced [*Weeks and Ackley*, 1982]. Since brine pockets move at different rates, one

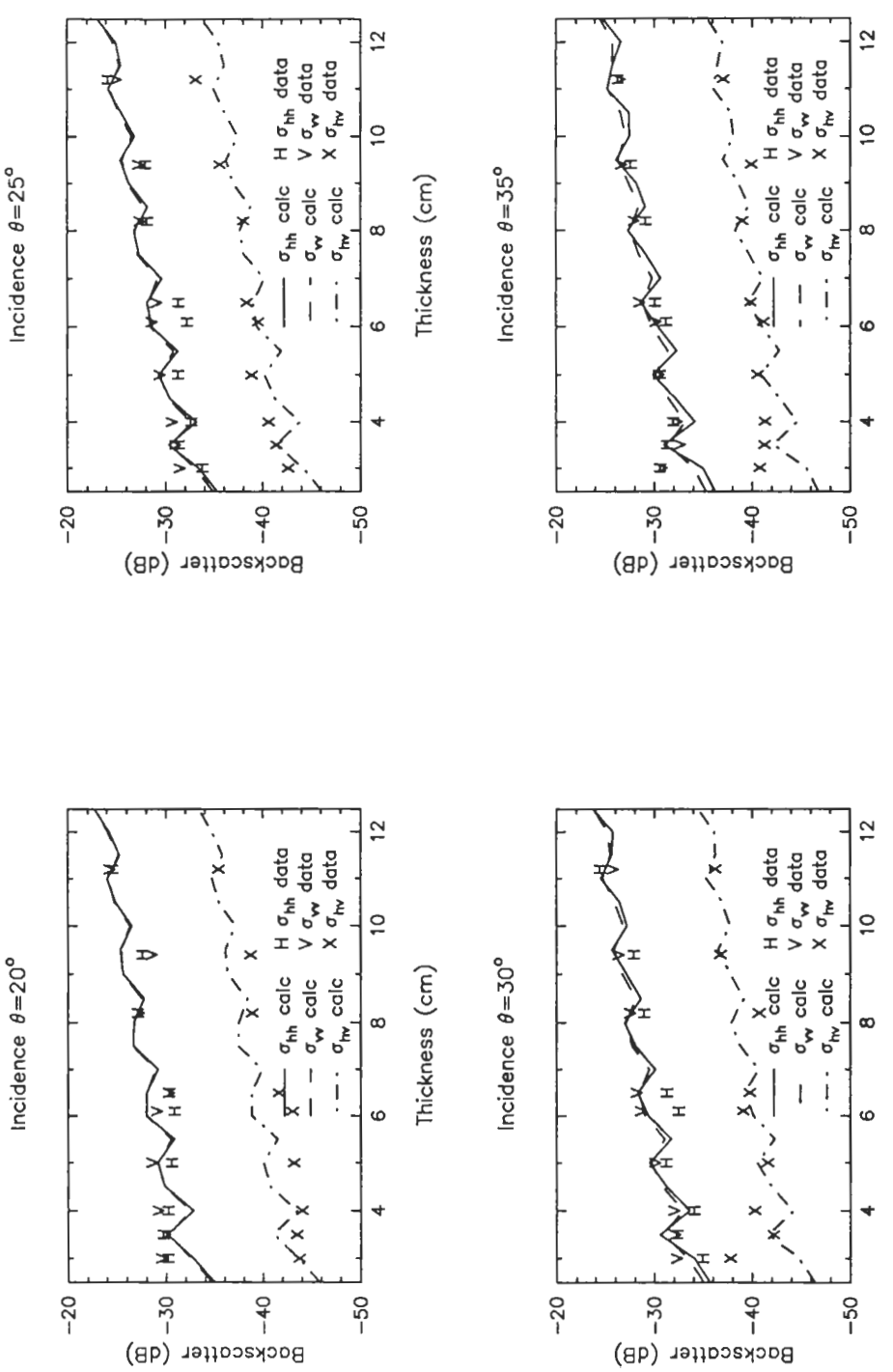

Figure 8. Measured data and calculated results for backscattering coefficients σ_{hh}, σ_{vv}, and σ_{hv} as functions of ice thickness at different incident angles. The calculated are obtained with uniform ice thicknesses at an average ice temperature of $-5°C$.

pocket can meet and combine or interconnect with another one to form a larger pocket. Consequently, the larger scatterers increase the backscatter.

An important desalinization mechanism is gravity drainage through brine channels. The physical process of the formation of brine drainage features in young sea ice is presented by *Eide and Martin* [1975]. Cold brine moves downward under the pressure gradient force as the ice grows thicker. The cold brine movement creates a total heat flux between the brine and the surrounding ice by the thermal gradient and by the eutectic boundary condition. The latter is shown to have the dominant effect [*Eide and Martin*, 1975], which occurs to keep the brine on the eutectic curve by the side-wall melting. This melting increases the radius of the brine features and thus causes the brine enlargement. It was not known in this experiment how much desalinization occurred owing to the gravity drainage mechanism; however, the enlargement of brine scatterers during the evolution of this desalinization mechanism conduces to the increase of backscatter from the young ice sheet.

It is noted that for brine scatterers that are much smaller than the wavelength (60 mm at 5 GHz), the Rayleigh scattering cross section is proportional to the sixth power of the scatterer size [*Kong*, 1986]. Thus the cross section increases significantly for a small increase in size. For example, a size doubling gives a 64-fold or 18-dB increase in the cross section. Nevertheless, scattering loss due to multiple wave interactions among scatterers needs to be accounted for to avoid an overemphasis on the backscatter increase. A complex model for sea ice accounting for scattering loss with strong permittivity fluctuations in the distorted Born approach [*Nghiem et al.*, 1995a] is necessary. The physical properties discussed in the above sections will be utilized in the modeling of saline ice to calculate polarimetric scattering coefficients.

4.3. Sea Ice Model

Wave propagation and polarimetric scattering models of sea ice have been extensively developed [*Nghiem et al.*, 1990, 1993a, 1995a, c]. The models account for effective attenuation including both absorption and scattering losses, thermodynamic phase distribution of constituents in sea ice, orientation distribution of crystallographic c axes, nonspherical geometry of brine scatterers and other inhomogeneities, anisotropy of columnar structure in sea ice, distribution in thickness of the ice sheet, multiple wave interactions with medium boundaries, and composite roughnesses at interfaces in layered media. Followed the scattering mechanisms discussed above, the model is simplified by using an anisotropic layered configuration with elongated ellipsoidal scatterers and planar interfaces for the saline ice sheet in this experiment.

The model is briefly reviewed here, and the necessary input parameters will be discussed in the next section. Polarimetric backscattering coefficients are defined by

$$\sigma_{\mu\tau\nu\kappa}(\theta) = \lim_{\substack{r\to\infty \\ A\to\infty}} \frac{4\pi r^2}{A} \frac{\langle E_{\mu s}(\theta) E^*_{\nu s}(\theta)\rangle}{E_{\tau i}(\theta) E^*_{\kappa i}(\theta)} \tag{4}$$

where E is an electric field; the asterisk denotes the complex conjugate; θ is the incident angle; subscripts μ, ν, τ, and κ can be h for horizontal polarization or v for vertical; subscripts i and s respectively stand for incident and scattered fields; r is the distance from the radar; and A is the illuminated area. The ensemble average of the scattered fields in (4) is determined by

$$\begin{aligned}\langle \bar{E}_s(\bar{r}) \bar{E}^*_s(\bar{r})\rangle = {} & \sum_{i,j,k,l,m}^{x,y,z} k_0^4 \int_0^\infty dd_1\, q_1(d_1) \int_0^\pi d\psi_{1f} \\ & \cdot \int_0^{2\pi} d\phi_{1f}\, p_1(\psi_{1f}, \phi_{1f}) \int_{V_1} d\bar{r}_1 \\ & \cdot \int_{V_1} d\bar{r}_1^o C_{1\xi jklm}(\bar{r}_1, \bar{r}_1^o; \psi_{1f}, \phi_{1f}) \\ & \cdot [\langle G_{01ij}(\bar{r}, \bar{r}_1)\rangle \langle F_{1k}(\bar{r}_1)\rangle] \\ & \cdot [\langle G_{01il}(\bar{r}, \bar{r}_1^o)\rangle \langle F_{1m}(\bar{r}_1^o)\rangle]^*\end{aligned} \tag{5}$$

where k_0 is the wave number in free space, q_1 is the probability density function of thickness d_1, ψ_{1f} and ϕ_{1f} are Eulerian angles used in p_1 to describe the scatterer orientation distribution, location $\bar{r}_1$ or $\bar{r}_1^o$ is in volume V_1 occupied by the inhomogeneous ice sheet, $\langle G\rangle$ is the mean dyadic Green's function of the anisotropic columnar ice, and $\langle F\rangle$ is the mean incident field. For the orientation the probability density function $p_1(\psi_{1f}, \phi_{1f}) = \sin\psi_{1f}/(4\pi)$ models the preferential vertical alignment in the columnar ice and random c axis directions in azimuth, as discussed in section 3.1.

Correlation function $C_{1\xi jklm}$ of the scatterer with variance Γ_{1jklm} is given by

$$C_{1\xi jklm}(\bar{r}_1, \bar{r}_1^o; \psi_{1f}, \phi_{1f})$$

$$= \langle \xi_{1jk}(\bar{r}_1)\xi_{1lm}^{*}(\bar{r}_1^o)|\psi_{1f}(\bar{r}_1), \phi_{1f}(\bar{r}_1)\rangle$$

$$= \int_{-\infty}^{\infty} d\bar{\beta}\, \Gamma_{1jklm}\Phi_{1\xi}(\bar{\beta}) \exp[-i\bar{\beta}(\bar{r}_1 - \bar{r}_1^o)] \qquad (6)$$

where $\Phi_{1\xi}$ is the normalized correlation function in the spectral domain. In the local coordinates (x', y', z'), $\Phi_{1\xi}$ is defined by

$$\Phi_{\xi}(\bar{k}') = \frac{l_{x'}l_{y'}l_{z'}}{\pi^2(1 + k_x'^2 l_{x'}^2 + k_y'^2 l_{y'}^2 + k_z'^2 l_{z'}^2)^2} \qquad (7)$$

in which $l_{x'}$, $l_{y'}$, and $l_{z'}$ are three different correlation lengths corresponding to the axes of an ellipsoidal scatterer in the local coordinates (x', y', z'), which relate to the global coordinates (x, y, z) by rotation transformations with orientation angles ψ_{1f} and ϕ_{1f}.

Inherent with the scattering effect, brine inclusions also influence electromagnetic wave propagation and attenuation. Thus the effect on wave propagation must be consistently treated with the same physical characteristics of the ice sheet. Wave propagation in the inhomogeneous columnar saline ice is characterized by an effective permittivity tensor with the effective optic axis in the vertical direction. Using the same physical parameters used in the backscatter calculations, the effective permittivity tensor is derived and has the form

$$\bar{\bar{\varepsilon}}_{1\text{eff}} = \bar{\bar{\varepsilon}}_{1g} + \varepsilon_0[\bar{\bar{I}} - \bar{\bar{\xi}}_{1\text{eff}}\langle\bar{\bar{S}}_1\rangle]^{-1}\bar{\bar{\xi}}_{1\text{eff}} \qquad (8)$$

where $\bar{\bar{I}}$ is the unit dyad and dyadic coefficient $\bar{\bar{S}}_1$ describes the polarizability of brine inclusions. The first term $\bar{\bar{\varepsilon}}_{1g}$ in (8) is for the quasi-static effect and the second term involving the effective dyadic scatterer $\bar{\bar{\xi}}_{1\text{eff}}$ represents the scattering effects in wave propagation. Permittivity tensor $\bar{\bar{\varepsilon}}_{1g}$ has the form of Polder-van Santen mixing formula related to permittivities of the constituents in the saline ice including background ice and brine inclusions. Effective dyadic scatterer $\bar{\bar{\xi}}_{1\text{eff}}$ is determined with the same correlation function used to calculate polarimetric scattering coefficients. Owing to the vertical preference of scatterers in the columnar structure, the saline ice is anisotropic, and effective permittivities of ordinary and extraordinary waves are different. Detail expressions for the effective permittivities and physical meanings of model parameters have been presented [*Nghiem et al.*, 1993a, 1995a].

4.4. Physical Parameters

In the calculations of effective permittivities and polarimetric backscatter, necessary input parameters are relative permittivity of air ($\varepsilon_0 = 1$), permittivity of ice determined from empirical formulas by *Vant et al.* [1978] or *Tiuri et al.* [1984], permittivity of brine by *Stogryn and Desargant* [1985], and permittivity of saline water by *Klein and Swift* [1977]. Another input parameter is fractional volume of brine obtained from measured temperature and salinity based on thermodynamic phase equations [*Cox and Weeks*, 1983].

Correlation lengths can be determined from geometrical characteristics of brine inclusions. However, no technique to directly measure in situ sizes and shapes of the inclusions was available for this experiment. Measurements from thin sections prepared from ice samples stored at −20°C only indicate lower bounds of correlation lengths. Instead, correlation length $l_{1x'} = 0.36$ mm is taken for the ice sheet at a 3-cm thickness. To calculate $l_{1y'}$ and $l_{1z'}$, axial ratios $l_{1x'}/l_{1y'} = 2.8$ and $l_{1z'}/l_{1x'} = 1.2$ are given [*Nghiem et al.*, 1995c]. To account for the size increase of brine scatterers during the desalination processes as discussed in section 4.2.3, a linear expansion rate of 0.0374 mm for a growth of 1 cm in ice thickness is used.

Measured values of ice thickness are not uniform over the ice sheet. Statistical descriptions of the ice thickness require a large number of thickness measurements at many locations on the ice sheet for all cases; this was not possible during scatterometer data acquisitions owing to time limitations and to the necessity of keeping characteristics of the ice sheet unperturbed. The model will be used to assess effects of thickness variations including uniform thickness, gamma distribution [*Nghiem et al.*, 1995b], and Gaussian distribution with a 10% standard deviation in the ice thickness.

The model is used to calculate both effective permittivities and polarimetric backscattering coefficients at incident angles ranging from 20° to 35° and mean ice thicknesses ranging from 3 to 12 cm. Input parameters for brine volume and permittivities are determined with experimental values of salinity and temperature. For a given temperature and salinity, permittivities of ice, brine, and seawater at the C band frequency are obtained from work cited above. The empirical linear function derived from the measured data in Figure 4 is used together with ice temperature in phase equations [*Cox and Weeks*, 1983] to determine the brine volume at each thickness. The tem-

Table 1. Input and Derived Parameters With Corresponding References

Input Parameters	References	Derived Parameters
f, T_{ice}	*Vant et al.* [1978]	$\mathrm{Re}(\varepsilon_{ice})$
f, T_{ice}	*Tiuri et al.* [1984]	$\mathrm{Im}(\varepsilon_{ice})$
f, T_{sea}, S_{sea}	*Klein and Swift* [1977]	$\mathrm{Re}(\varepsilon_{sea})$, $\mathrm{Im}(\varepsilon_{sea})$
f, T_{ice}	*Stogryn and Desargant* [1985]	$\mathrm{Re}(\varepsilon_{brine})$, $\mathrm{Im}(\varepsilon_{brine})$
T_{ice}, S_{ice}	*Cox and Weeks* [1983]	f_{brine}
Thickness	this paper	d_1 (measured)

Here f, wave frequency; T, temperature; S, salinity; Re, real part; Im, imaginary part; ε, relative permittivity; f_{brine}, fractional volume of brine; and d_1, thickness of the saline ice sheet.

perature of the ice sheet averaged −5°C with variations within ±1°C, which will be considered in model calculations.

As a summary, the input and derived parameters are listed in Table 1. The parameters are measured or determined from published results in the references shown in Table 1. The predetermined parameters and the initial value and expansion rate of $l_{1x'}$ given above are used in the theoretical model. The model results have to explain all the polarimetric measurements, as functions of incident angles, and their trends over the successive stages of the saline ice growth.

4.5. Data Comparisons

Theoretical results are compared with experimental data for all five independent polarimetric parameters including σ_{hh}, σ_{vv}, σ_{hv}, magnitude of ρ, and phase of ρ as functions of incident angles. The comparisons are shown in Figure 7. In this example the average ice thickness is 8.2 cm with the Gaussian distribution (10% standard deviation; see section 4.4). Calculated results and experimental data compare well for the five polarimetric coefficients at all of the incident angles. The exception is ρ at 35°, where the measured magnitude and phase of ρ are lowered than the predicted values. The weak dependence of backscattering coefficients on incident angle is intrinsic to the scattering characteristics of brine inclusions in the ice volume [*Nghiem et al.*, 1993a]. Uncertainties caused by ±1°C in ice temperature are represented by vertical error bars. The temperature uncertainties yield backscatter deviations of only 1 dB and have little effect on the complex correlation coefficients. Another example of the comparisons over incident angles for the same ice sheet at a thickness of 11.2 cm is given by *Nghiem et al.* [1995c].

Over the entire thickness range observed during the ice growth, comparisons of calculated and measured backscattering coefficients are made for all cases and presented in Figures 8–10. Figure 8 is for the case of uniform thickness. In general, calculated results compare fairly well with measured data. Furthermore, the model results track the increasing trend observed in the experimental backscatter. Oscillations in backscatter obtained from the uniform thickness ice model result from multiple interactions of electromagnetic waves between the planar interfaces of the ice sheet [*Nghiem et al.*, 1990, 1993a].

The case for ice thickness with the gamma distribution is shown in Figure 9. This model also indicates the increasing trend in all backscattering coefficients, as seen also in Figure 9. However, the sensitivity of backscatter with thickness is weaker and the increase is up to only 6 dB over the entire thickness range. This is because the gamma distribution has a long tail, allowing probabilistic realizations with large thicknesses to exist even in the case of a small mean thickness. This case is not representative of the ice sheet grown in the laboratory; however, it is presented here to show the effect of the gamma-distributed thickness on backscatter and also to suggest that a narrower distribution of thickness such as the Gaussian distribution should be more appropriate.

Figure 10 shows backscatter for the case of thickness with the Gaussian distribution. Calculated and measured values of the backscattering coefficients as well as the increasing trend during the ice growth are in good agreement. For distributed ice thicknesses, coherent effects responsible for oscillations in theoretical backscatter curves are suppressed by an averaging effect on phases of both incident and scattered waves. In Figures 9 and 10, the uncertainties due to ±1°C in ice temperature are also shown. The figures show that variations in σ_{hh} and σ_{vv} are smaller than those in σ_{hv}. Variations caused by ±1‰ uncertainties in bulk salinity are also investigated. The results show even smaller variations in backscatter.

Finally, backscattering coefficients for the 11.2-cm-thick saline ice are compared with the JPL airborne C band SAR measurements. The airborne SAR data were acquired over thin sea ice growing in a newly opened lead in the Beaufort Sea [*Nghiem et al.*, 1995b]. The results presented in Figure 11 show that both copolarized and cross-polarized backscattering coefficients of thin ice grown in the laboratory and occurring naturally in the Arctic are generally similar. At small incident angles around 25°, copolarized backscatter of the lead ice is slightly larger (see Figure

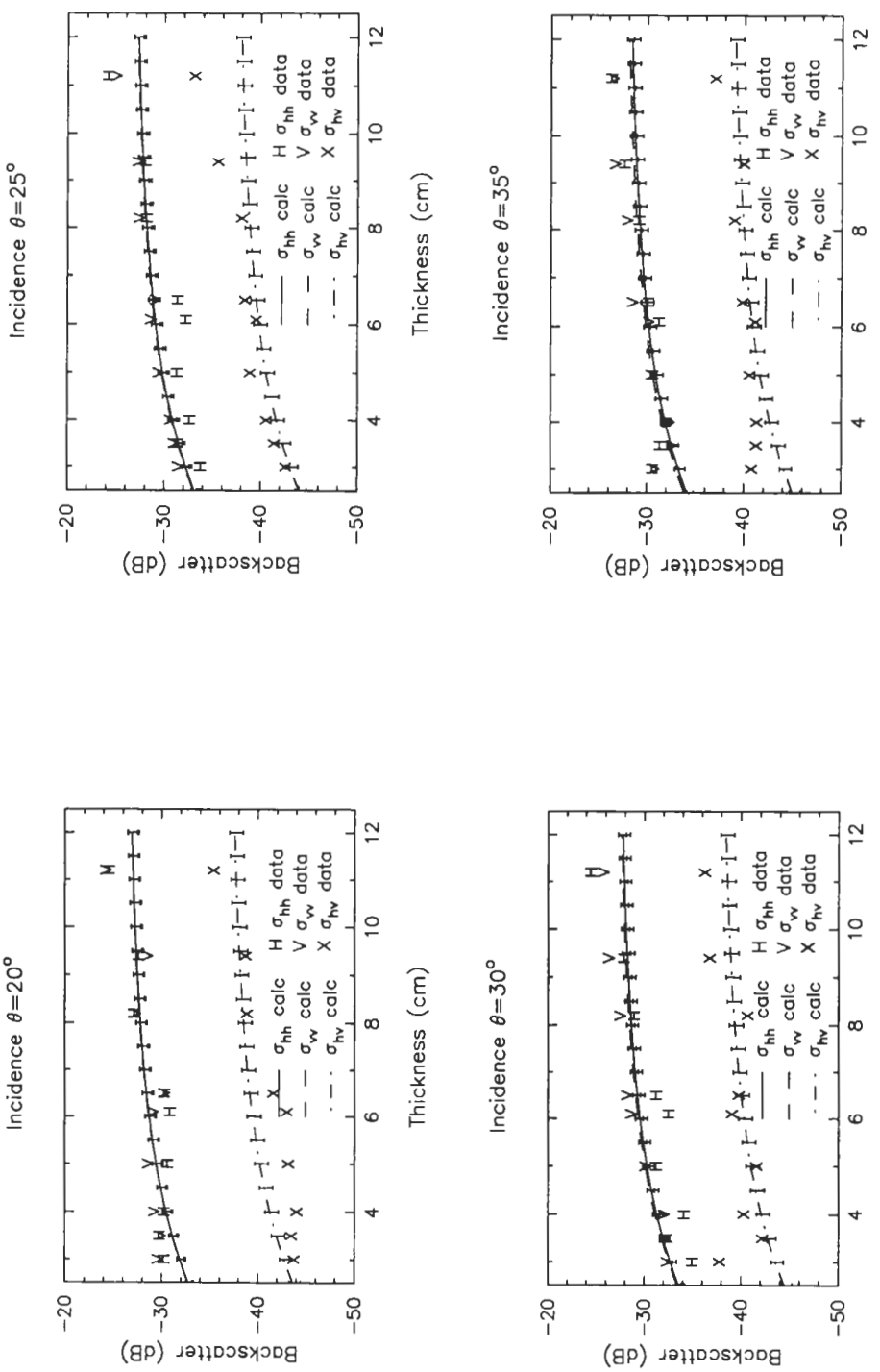

Figure 9. Measured data and calculated results for backscattering coefficients σ_{hh}, σ_{vv}, and σ_{hv} as functions of ice thickness at different incident angles. The calculated values are obtained with gamma-distributed ice thicknesses with a ±1°C uncertainty in ice temperature.

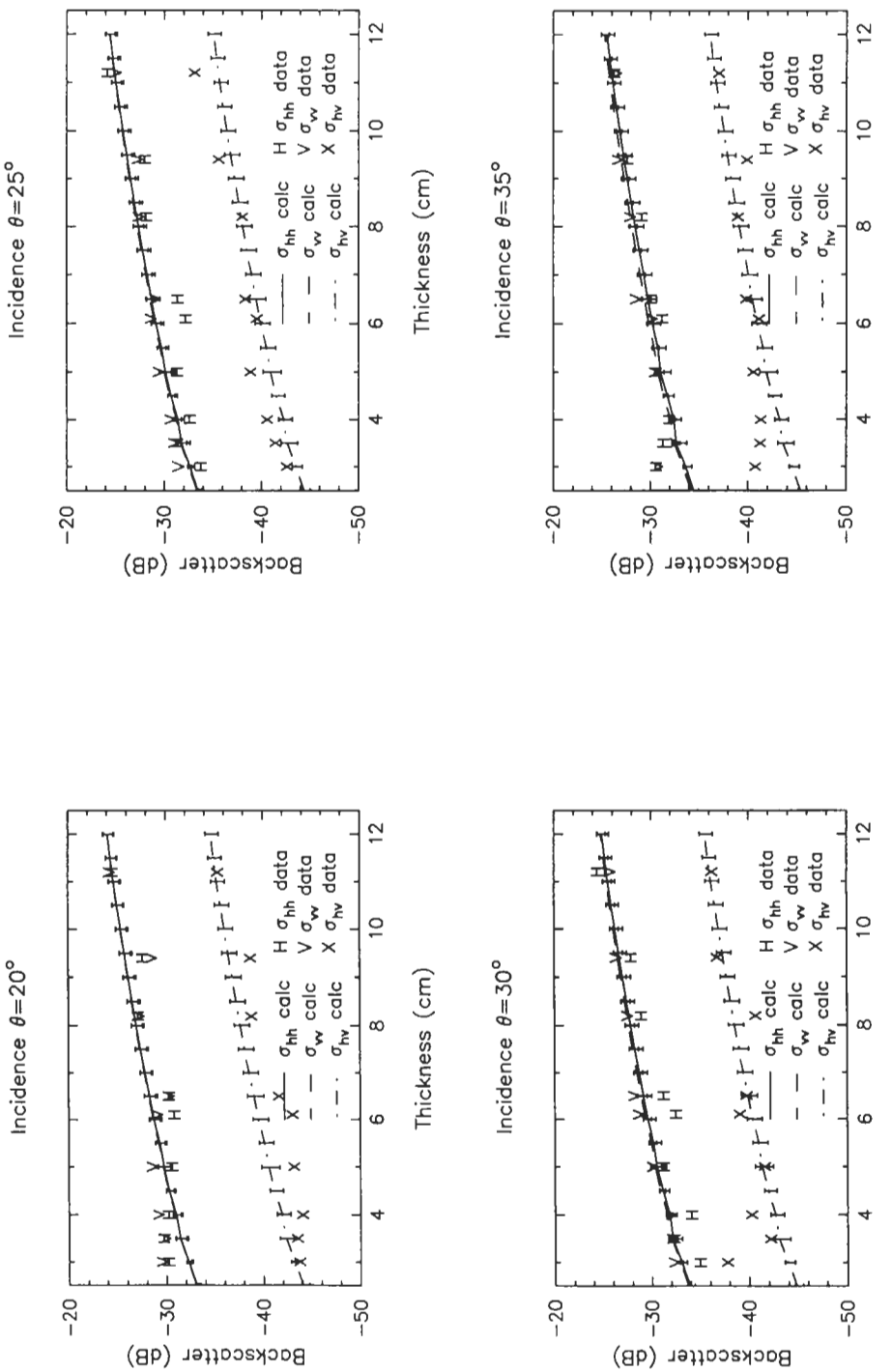

Figure 10. Measured data and calculated results for backscattering coefficients σ_{hh}, σ_{vv}, and σ_{hv} as functions of ice thickness at different incident angles. The calculated are obtained with Gaussian-distributed ice thicknesses with ± 1°C uncertainty in ice temperature.

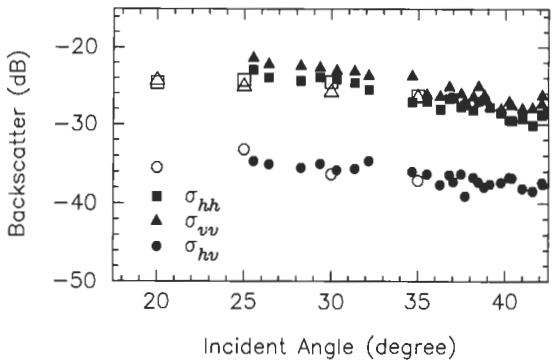

Figure 11. Comparison of backscattering coefficients for 11.2-cm-thick saline ice with airborne SAR measurements of thin sea ice in a newly opened lead in the Beaufort Sea. Solid symbols are for the sea ice, and open ones are for the saline ice, with σ_{hh} denoted by squares, σ_{vv} denoted by triangles, and σ_{hv} denoted by circles.

11) than that of the laboratory ice, which represents a lower backscatter level corresponding to the smooth surface of the ice sheet grown under quiescent conditions.

5. Summary

In this paper we have presented both the physical characteristics and polarimetric scattering properties of a saline ice sheet grown at a constant growth rate under quiescent conditions. The objectives of the experiment were (1) to identify the electromagnetic interaction mechanism in the saline ice sheet, (2) to relate the wave-scattering properties to ice physical characteristics, and (3) to assess the ice thickness inversion from backscatter data. In addition, both ice characteristics and radar backscatter obtained in this experiment have been compared to Arctic measurements to evaluate the feasibility of using laboratory environments to investigate radar backscatter for remote sensing of sea ice. C band polarimetric backscatter data at different incident angles were taken throughout the growth process together with ice characterization measurements. This data set imposes restrictions on the analysis in this paper, which has to be consistent with interrelated physical properties and processes intrinsic to the saline ice growth.

Physical characteristics of the ice sheet including growth conditions, thickness and growth rate, temperatures and salinities, and internal and interfacial structures were described. The characteristics of the saline ice grown in this experiment compare well with Arctic sea ice grown under similar environmental conditions. Polarimetric backscattering coefficients measured during the ice growth reveal a significant increase by 6–10 dB for ice thickness ranging from 3 to 11.2 cm. With observed physical characteristics and processes pertaining to the ice growth the large enhancement in the backscatter is suggested to relate to an increase in the effective scatterer size caused by brine interconnections and wall melting during the desalinization process. For these small-scale brine scatterers, backscatter is still sensitive to the size increase with due consideration also to multiple wave interaction effects in the scattering loss.

Polarimetric signatures calculated with a sea ice model with physical parameters describing ice characteristics compare well with polarimetric backscatter measurements over the range of incident angles from 20° to 35° and for all successive stages of the ice growth. Backscattering coefficients of the saline ice sheet are also shown to be consistent with airborne radar measurements of the thin sea ice type in a newly opened lead in the Beaufort Sea. Furthermore, ice thickness in this experiment is retrievable from scatterometer measurements because of the strong increasing trend observed in the backscattering coefficients. In polar oceans, saline ice grows under complicated conditions of wind and wave interactions, temperature variations, frost flower formation, and snow cover. These complex conditions with associated physical processes can be investigated in future experiments.

Appendix A: Data Processing

This appendix describes the polarimetric data processor of the C band system. To maximize the data acquisition capacity of the system, an algorithm for data compression is implemented in the data acquisition mode of the scatterometer-controlling software with negligible quantization errors. In the data processor, raw data are first decompressed to obtain magnitudes and phases in the frequency domain. For each incident and azimuth angle, 20 sets of measurements with 401 frequency samples in the 1-GHz bandwidth are coherently averaged. For each target, system background noises are coherently subtracted from total signals to increase the signal-to-noise ratio of the targets. This technique was used to detect a single small pin 3.8 m away from the antenna, as demonstrated in the Sea Ice Electromagnetics Workshop in 1993 [*Nghiem*, 1993]. An important feature

required for this technique to work is the preservation of the system phase between background and target measurements. This is considered in the hardware design and measurement deployment of the C band system. Moreover, to achieve a low noise floor, the system is designed such that the return from the target range is located in the "valley" between the first and second reflections from the antenna feed and other RF components.

An optimum resolution and sidelobe level are achieved with the Hamming window, which is selected over choices of rectangular, Hanning, and several Kaiser-Bessel windows. The fast Fourier transform is applied to obtain time domain data, which are gated to isolate target signals. Effects of discrete sampling, picket fence, and frequency band limit are considered. The system transfer function accounting for the processor gain pattern is obtained for signal reconstructions. Simulations for different target types, such as point target, multiple target, and distributed target, are carried out to test the signal reconstruction process. The data are calibrated both polarimetrically and radiometrically (see Appendix B). To obtain backscattering coefficients, full three-dimensional antenna patterns and directivity or absolute antenna gain for the C band system (see Appendix C) are determined for all transmit and receive ports and polarizations (including copolarization and cross polarization) over the 1-GHz frequency band. An algorithm is developed using the full antenna patterns, tested with end-to-end simulations, and applied to measured data for pattern deconvolution in the determination of backscattering coefficients.

Appendix B: Calibrations

Trihedral corner reflectors and a sphere are used to calibrate the system. The corner reflectors are aligned to the antenna look direction with a laser pointer. Polarimetric calibrations consider cross talk, reciprocity, channel imbalance in amplitude, and phase. Polarimetric calibration measurements indicate an overall cross-talk level of about -25 dB. The system is very well reciprocal within a fraction of 1 dB in magnitude and a few degrees in phase. Horizontal and vertical channels are not perfectly balanced, and calibration target measurements provide data to balance the channels. For this system the channel balance is within 0.2 dB. All radar cross sections of the trihedral corner reflectors and the sphere are known. These cross sections are used to cross-check each other and to calibrate the system for absolute gain. The calibrated gain is consistent with the gain estimated from component gains and losses in the system. The overall backscatter error bar is estimated at ± 1.2 dB for the radar configuration used in this experiment.

Before the experiment the system was checked with the quick-look mode for trihedral and sphere measurements to ensure the performance of the system. Throughout the experiment, polarimetric measurements were carried out to collect data for calibration purposes. Calibration measurements included the corner reflectors, the sphere, external backgrounds, and internal system measurements. These measurements were made periodically throughout the experiment for consideration of the scatterometer system stability.

Appendix C: Antenna Patterns and Directivity

For a radar system with an extremely small beamwidth approaching the so-called plane-wave condition, which is characterized with a Dirac delta function of the antenna beam angle, the backscattering coefficient can be taken out of the integration in the radar equation. Such a system is not useful for most remote sensing applications which require a large radar swath width. In this case a practical radar system has a larger beamwidth and the antenna patterns need to be determined to deconvolute the pattern effects from the backscattering coefficient. It is in this regard that the antenna patterns of the C band scatterometer are presented here.

Antenna patterns for copolarization and cross polarization were measured at E, H, $+45°$ (P), and $-45°$ (Q) planes at 4.5, 5.0, and 5.5 GHz. Pattern measurements were cut off at -30 dB for copolarization and -40 dB for cross polarization. However, complete three-dimensional (3-D) antenna patterns are necessary for the pattern deconvolution algorithm to account for the beam effects in determining polarimetric backscattering coefficients from the radar equation. The 3-D patterns are calculated with Fresnel integrations [*Balanis*, 1982] together with the superposition method [*Love*, 1962] to achieve a better accuracy. Calculated patterns compare very well with measured data, as shown in Figure 12, for the horizontal port at 5 GHz in E, H, P, and Q planes. Good comparisons are also obtained at 4.5 and 5.5 GHz and for the vertical port.

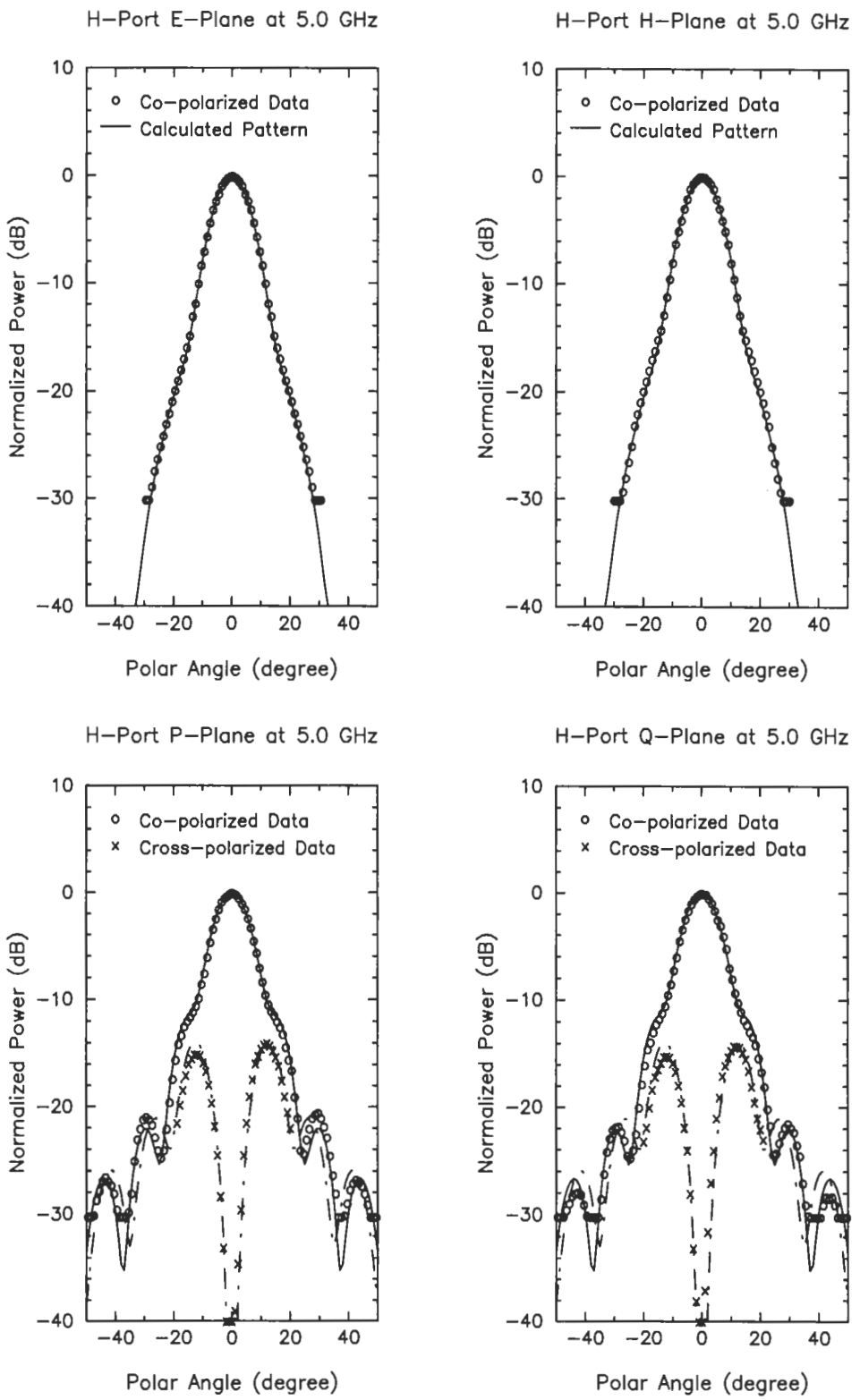

Figure 12. Antenna patterns for the horizontal port at E, H, P, and Q planes. Symbols are for measured data and curves are for calculated values.

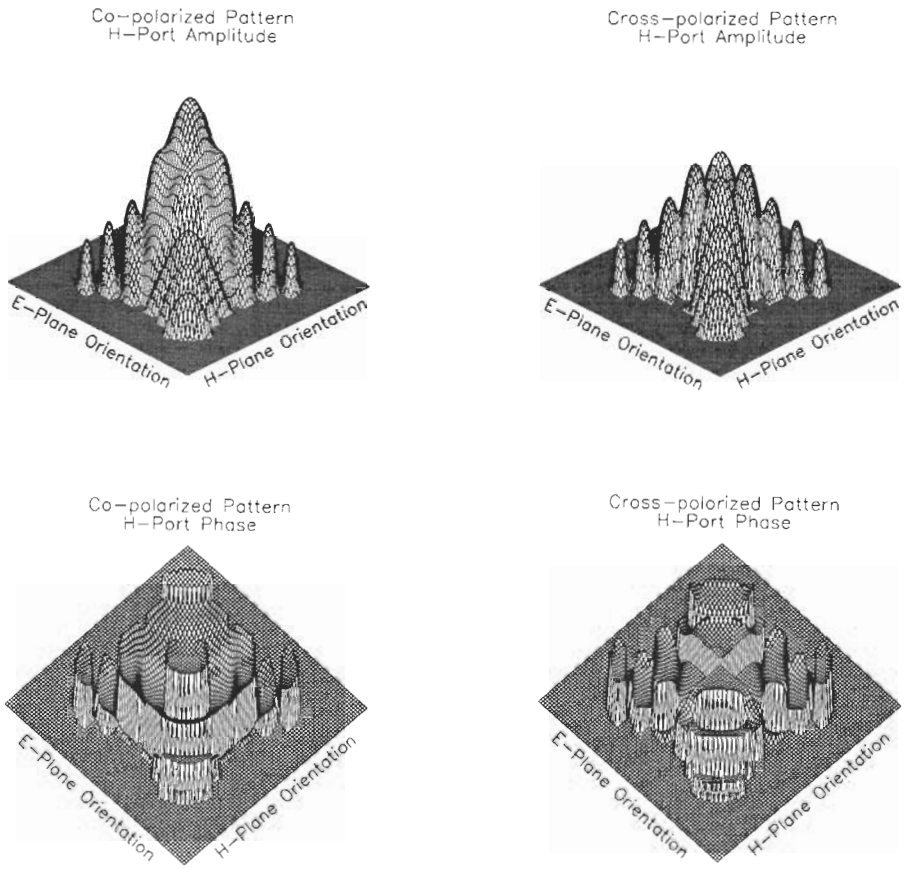

Figure 13. Three-dimensional antenna patterns for the horizontal port and for both copolarization and cross polarization. To optimize the three-dimensional illustration, amplitude and phase patterns are shown at different viewing angles.

Figure 13 shows magnitudes (decibels) and phases (degrees) of the copolarized and cross-polarized 3-D antenna patterns for horizontal polarization (H-port excitation). The 3-D patterns for the vertical polarization are the same. This is because of the antenna symmetry. The one-way sidelobe level is about 22 dB below the peak gain. There is no observable cross polarization in the principal planes. The maximum cross-polarized level is in the $\pm 45°$ plane. When multiplied to the corresponding copolarization pattern, the maximum cross polarization results in a cross-polarized magnitude of -25 dB. It is noted that the cross-polarized phase is antisymmetric (see Figure 13). Consequently, the cross-polarization contamination is smaller for targets with reflection or azimuthal symmetry, such as columnar saline ice with c axes randomly oriented in azimuth. From the 3-D patterns the gain with respect to isotropic radiation (directivity) is calculated to be within 0.3 dB of all measured values at 4.5, 5.0, and 5.5 GHz.

Acknowledgments. The research described in this paper was performed by the Center for Space Microelectronics Technology, Jet Propulsion Laboratory, California Institute of Technology, and was sponsored by the Office of Naval Research (ONR) through an agreement with the National Aeronautics and Space Administration. The research by the U.S. Army CRREL was under ONR contracts N00014-95-MP-3002 and N00014-95-MP-3019, and that by the Massachusetts Institute of Technology under ONR contracts N00014-89-J-1107 and N00014-92-J-4098.

References

Adams, C. M., Jr., D. N. French, and W. D. Kingery, Solidification of sea ice, *J. Glaciol.*, *3*, 745–760, 1960.

Balanis, C. A., *Antenna Theory Analysis and Design*, Harper and Row, New York, 1982.

Beaven, S. G., G. L. Lockhart, S. P. Gogineni, A. R. Hosseinmostafa, K. Jezek, A. J. Gow, D. K. Perovich, A. K. Fung, and S. Tjuatja, Laboratory measurements of radar backscatter from bare and snow-covered saline ice sheets, *Int. J. Remote Sens.*, *16*(5), 851–876, 1995.

Carsey, F., Science requirements for RADARSAT/ERS-2 modifications for the Alaska SAR facility, *JPL Doc. D-10443*, Jet Propul. Lab., Pasadena, Calif., 1993.

Cavalieri, D. J., J. P. Crawford, M. R. Drinkwater, D. T. Eppler, L. D. Farmer, R. R. Jentz, and C. C. Wackerman, Aircraft active and passive microwave validation of sea ice concentration from the Defense Meteorological Satellite Program Special Sensor Microwave Imager, *J. Geophys. Res.*, *96*(C12), 21,989–22,008, 1991.

Cox, G. F. N., Brine drainage in sodium chloride ice, Ph.D. thesis, Dartmouth Coll., Hanover, N. H., 1974.

Cox, G. F. N., and W. F. Weeks, Salinity variations in sea ice, *J. Glaciol.*, *13*(67), 109–120, 1974.

Cox, G. F. N., and W. F. Weeks, Equations for determining the gas and brine volumes in sea-ice samples, *J. Glaciol.*, *29*(12), 306–316, 1983.

Eide, L. I., and S. Martin, The formation of brine drainage features in young sea ice, *J. Glaciol.*, *14*(70), 137–154, 1975.

European Space Agency, (ESA), The ERS-1 system, *ESA SP-1146*, Neuilly, France, 1992.

Fukusako, S., Thermophysical properties of ice, snow, and sea ice, *Int. J. Thermophys.*, *11*(2), 353–372, 1990.

Gardini, B., G. Graf, and G. Ratier, The instruments on ENVISAT, *Acta Astronaut.*, *37*, 301–311, 1995.

Gow, A. J., and W. F. Weeks, The internal structure of fast ice near Narwhal Island, Beaufort Sea, Alaska, *CRREL Rep. 77-29*, U.S. Army Corps of Eng., Cold Reg. Res. and Eng. Lab., Hanover, N. H., 1977.

Gow, A. J., S. A. Arcone, and S. G. McGrew, Microwave and structural properties of saline ice, *CRREL Rep. 87-20*, U.S. Army Corps of Eng., Cold Reg. Res. and Eng. Lab., Hanover, N. H., 1987.

Kingery, W. D., and W. H. Goodnow, Brine migration in salt ice, in *Ice and Snow: Properties, Processes, and Applications*, edited by W. D. Kingery, chap. 19, pp. 237–247, MIT Press, Cambridge, Mass., 1963.

Klein, L. A., and C. Swift, An improved model for the dielectric constant of sea water at microwave frequencies, *IEEE Trans. Antennas Propag.*, *25*(1), 104–111, 1977.

Kong, J. A., *Electromagnetic Wave Theory*, John Wiley, New York, 1986.

Kuester, J. L., and J. H. Mize, *Optimization Techniques with Fortran*, McGraw-Hill, New York, 1973.

Kwok, R., and G. F. Cunningham, Backscatter characteristics of the winter ice cover in the Beaufort Sea, *J. Geophys. Res.*, *99*(C4), 7787–7802, 1994.

LeadEx Group, The LeadEx Experiment, *Eos Trans. AGU*, *74*(35), 393, 1993.

Lofgren, G., and W. F. Weeks, Effect of growth parameters on substructure spacing in NaCl ice crystals, *Res. Rep. 195*, Cold Reg. Res. and Eng. Lab., U.S. Army Terr. Sci. Cent., Hanover, N. H., 1969.

Love, A. W., The diagonal horn antenna, *Microwave J.*, 117–122, 1962.

Marquardt, D. W., An algorithm for least-squares estimation of nonlinear parameters, *J. Soc. Indust. Appl. Math.*, *11*, 431–441, 1963.

Maykut, G. A., Energy exchange over young sea ice in the central Arctic, *J. Geophys. Res.*, *83*(C7), 3646–3658, 1978.

Moritz, R. E., J. A. Curry, A. S. Thorndike, and N. Untersteiner (Eds.), Surface heat budget of the Arctic Ocean, *Rep. 3*, Polar Sci. Cent., Appl. Phys. Lab., U. of Wash., Seattle, 1993.

Nakawo, M., and N. K. Sinha, A note on brine layer spacing of first-year sea ice, *Atmos. Ocean*, *22*(2), 193–206, 1984.

Nghiem, S. V., C-band polarimetric scatterometer: System, operation, sensitivity and calibration, paper presented at Sea Ice Electromagnetics Workshop, Off. of Nav. Res., Hanover, N. H., Sept. 14–16, 1993.

Nghiem, S. V., M. Borgeaud, J. A. Kong, and R. T. Shin, Polarimetric remote sensing of geophysical media with layer random medium model, in *Progress in Electromagnetics Research*, vol. 3, *Polarimetric Remote Sensing*, edited by J. A. Kong, chap. 1, pp. 1–73, Elsevier, New York, 1990.

Nghiem, S. V., S. H. Yueh, R. Kwok, and F. K. Li, Symmetry properties in polarimetric remote sensing, *Radio Sci.*, *27*(5), 693–711, 1992.

Nghiem, S. V., R. Kwok, J. A. Kong, and R. T. Shin, A model with ellipsoidal scatterers for polarimetric remote sensing of anisotropic layered media, *Radio Sci.*, *28*(5), 687–703, 1993a.

Nghiem, S. V., S. H. Yueh, R. Kwok, and D. T. Nguyen, Polarimetric remote sensing of geophysical medium structures, *Radio Sci.*, *28*(6), 1111–1130, 1993b.

Nghiem, S. V., R. Kwok, S. H. Yueh, and M. R. Drinkwater, Polarimetric signatures of sea ice, 1, Theoretical model, *J. Geophys. Res.*, *100*(C7), 13,665–13,679, 1995a.

Nghiem, S. V., R. Kwok, S. H. Yueh, and M. R. Drinkwater, Polarimetric signatures of sea ice, 2, Experimental observations, *J. Geophys. Res.*, *100*(C7), 13,681–13,698, 1995b.

Nghiem, S. V., R. Kwok, S. H. Yueh, J. A. Kong, C. C. Hsu, M. A. Tassoudji, and R. T. Shin, Polarimetric scattering from layered media with multiple species of scatterers, *Radio Sci.*, *30*(4), 835–852, 1995c.

Onstott, R. G., Polarimetric radar measurements of artificial sea ice during CRREL-EX'88, *ERIM Tech. Rep. 196100-23-T*, Environ. Res. Inst. of Mich., Ann Arbor, 1990.

Shih, S. E., K. H. Ding, S. V. Nghiem, C. C. Hsu, J. A. Kong, and A. K. Jordan, Thickness retrieval using time series

electromagnetic measurements of laboratory grown saline ice, *Proc. Int. Geosci. Remote Sens. Symp.*, vol. II, pp. 1208–1210, IEEE, Piscataway, N. J., 1996.

Stogryn, A., and G. J. Desargant, The dielectric properties of brine in sea ice at microwave frequencies, *IEEE Trans. Antennas Propag.*, *33*(5), 523–532, 1985.

Thorndike, A. S., D. A. Rothrock, G. A. Maykut, and R. Colony, The thickness distribution of sea ice, *J. Geophys. Res.*, *80*(33), 4501–4513, 1975.

Tiuri, M. E., A. H. Sihvola, E. G. Nyfors, and M. T. Hallikainen, The complex dielectric constant of snow at microwave frequencies, *IEEE J. Ocean Eng.*, *9*(5), 377–382, 1984.

Tsang, L., J. A. Kong, and R. T. Shin, *Theory of Microwave Remote Sensing*, John Wiley, New York, 1985.

Vant, M. R., R. O. Ramseier, and V. Markios, The complex dielectric constant of sea ice at frequencies in the range 0.1–40 GHz, *J. Appl. Phys.*, *49*(3), 1264–1280, 1978. (Erratum, *J. Appl. Phys.*, *53*(2), 1269, 1982).

Wakatsuchi, M., and N. Ono, Measurements of salinity and volume of brine excluded from growing sea ice, *J. Geophys. Res.*, *88*(C5), 2943–2951, 1983.

Weeks, W. F., and S. F. Ackley, *The Growth, Structure, and Properties of Sea Ice*, *Monogr. Ser.*, vol. 82-1, U.S. Army Corps of Eng., Cold Reg. Res. and Eng. Lab., Hanover, N. H., 1982.

Yen, Y. C., Review of thermal properties of snow, ice, and sea ice, *CRREL Rep. 81-10*, U.S. Army Corps of Eng., Cold Reg. Res. and Eng. Lab., Hanover, N. H., 1981.

A. J. Gow and D. K. Perovich, U.S. Cold Regions Research and Engineering Laboratory, 72 Lyme Rd., Hanover, NH, 03755.

C. C. Hsu and J. A. Kong, Department of Electrical Engineering and Computer Science and Research Laboratory of Electronics, Massachusetts Institute of Technology, 77 Massachusetts Ave., Rm. 26-305, Cambridge, MA 02139.

R. Kwok, S. V. Nghiem, and S. H. Yueh, Center for Space Microelectronics Technology, Jet Propulsion Laboratory, California Institute of Technology, Mail Stop 300-235, 4800 Oak Grove Dr., Pasadena, CA 91109. (e-mail: nghiem@malibu.jpl.nasa.gov)

(Received June 4, 1996; revised September 23, 1996; accepted October 4, 1996.)